crystals

MDPI

Review

High-Entropy Engineering in Thermoelectric Materials: A Review

Subrata Ghosh [1], Lavanya Raman [2], Soumya Sridar [3] and Wenjie Li [1,*]

[1] Department of Materials Science and Engineering, Pennsylvania State University, University Park, PA 16802, USA; smg7204@psu.edu
[2] Department of Mechanical Engineering, University of Wisconsin-Madison, Madison, WI 53706, USA; lraman@wisc.edu
[3] Department of Mechanical Engineering and Materials Science, University of Pittsburgh, Pittsburgh, PA 15261, USA; sos57@pitt.edu
* Correspondence: wzl175@psu.edu

Abstract: Thermoelectric (TE) materials play a crucial role in converting energy between heat and electricity, essentially for environmentally friendly renewable energy conversion technologies aimed at addressing the global energy crisis. Significant advances in TE performance have been achieved over the past decades in various TE materials through key approaches, such as nanostructuring, band engineering, and high-entropy engineering. Among them, the design of high-entropy materials has recently emerged as a forefront strategy to achieve significantly low thermal conductivity, attributed to severe lattice distortion and microstructure effects, thereby enhancing the materials' figure of merit (zT). This review reveals the progress of high-entropy TE materials developed in the past decade. It discusses high-entropy-driven structural stabilization to maintain favorable electrical transport properties, achieving low lattice thermal conductivity, and the impact of high entropy on mechanical properties. Furthermore, the review explores the theoretical development of high-entropy TE material and discusses potential strategies for future advancements in this field through interactions among experimental and theoretical studies.

Keywords: high-entropy engineering; thermoelectric; figure of merit; chalcogenides; half-Heusler; low thermal conductivity

Citation: Ghosh, S.; Raman, L.; Sridar, S.; Li, W. High-Entropy Engineering in Thermoelectric Materials: A Review. *Crystals* **2024**, *14*, 432. https://doi.org/10.3390/cryst14050432

Academic Editor: Andrei Vladimirovich Shevelkov

Received: 15 April 2024
Revised: 27 April 2024
Accepted: 27 April 2024
Published: 30 April 2024

1. Introduction

High-entropy alloys (HEAs) have recently gained popularity in the diverse fields of structural materials owing to their potential for remarkable mechanical properties compared to conventional alloys, such as a better strength-to-weight ratio, higher fracture resistance, higher tensile strength, and higher corrosion resistance [1,2]. In 2004, Yeh and Cantor introduced the idea of designing HEAs or multicomponent alloys (MCAs) using elements in equiatomic or near-equiatomic proportions to increase the entropy of mixing [3,4]. HEAs are usually produced by mixing five or more elements in equimolar ratios or nearly equal proportions, with at least one element of 5–35% molar percentage at a single crystallographic site [3]. The crystal phase of HEAs stabilizes at an elevated temperature through the reduction of Gibbs free energy (G), while the mixing entropy of the system (ΔS) dominates the enthalpy (H) of the system. Usually, the multicomponent materials associated with ΔS greater than $1.5R$ (R is the molar gas constant, 8.31 J mol^{-1}K^{-1}) are considered HEAs. ΔS is determined by four factors: configurational (ΔS_{conf}), electronic randomness, magnetic dipole, and vibrational entropy. However, ΔS_{conf} holds more weight than the other three factors [5]. The Boltzmann equation governs ΔS_{conf}, which determines how the available energy is shared among the atoms in a system. The ΔS_{conf} per mole for the formation of a solid solution from n elements with mole fraction x_i is calculated using the following equation:

$$\Delta S_{conf} = -R\sum_{i=1}^{n} x_i ln x_i \quad (1)$$

So far, the concept of high-entropy engineering has also been applied successfully in various functional material fields, such as catalysis [6] and dielectrics [7], and more recently in thermoelectrics (TE) [8–12].

Thermoelectric generators (TEGs) represent a direct energy conversion between heat and electricity, which shows promise in harvesting green energy from waste heat and provides an alternative to conventional cooling technology [8,9,13–18]. TE conversion efficiency (η) of a TEG primarily depends on the TE material's dimensionless average figure of merit (zT_{avg}) under a temperature gradient ($\Delta T = T_h - T_C$; T_h and T_C are the hot-side and cold-side temperature of a TEG device, respectively) as [19–21] follows:

$$\eta = \frac{T_h - T_c}{T_h} \frac{\sqrt{1 - zT_{avg}} - 1}{\sqrt{1 - zT_{avg}} + T_c/T_h} \quad (2)$$

The figure of merit (zT) of a TE material is derived from $zT = \frac{S^2\sigma T}{\kappa}$, where S is the Seebeck coefficient, σ is electrical conductivity, T is absolute temperature, and κ is the total thermal conductivity, the sum of the electronic (κ_{el}) and lattice (κ_L) parts of thermal conductivity. To achieve a high zT, a high power factor ($S^2\sigma$) or/and a low κ are required, which is expected in a semiconductor's typical carrier concentration (n) range, 10^{19}–10^{21} cm^{-3} (Figure 1a) [22]. However, enhancing the zT value is a challenge due to the intercorrelation among these TE parameters (S, σ, κ). Various effective approaches have been implemented to decouple electron and phonon transport behaviors in order to maximize the zT of TE materials. The two main strategies are: (i) the band engineering approach to optimize the electric transport properties by increasing the density-of-states effective mass [22–24], and (ii) the nanostructuring approach to reduce κ_L by increasing strong phonon scattering [14,25–27].

Recently, entropy engineering in TE materials has emerged as a promising avenue to enhance the performance of materials. In this context, the TE properties of HEAs are manipulated through not only the individual constituent elements but also their mutual interactions. The presence of multiple elements in HEAs with different atomic masses and ionic radii would introduce severe lattice distortion in a short-range order (Figure 1b) [28]. Consequently, it impacts the scattering of heat-carrying phonons. Thus, the κ_L of HEAs can be reduced significantly. Moreover, HEAs usually prefer to form crystal phases with high symmetry, which typically have electronic bands with multivalley features. As a result, it increases the electronic density-of-states effective mass, leading to a high S. The feasibility of improving the zT value by achieving a low κ_L and high S in HEAs using different TE materials has sought the attention of the TE community. This approach has been successfully utilized mainly in chalcogenide-based systems. For example, Jiang et al. reported a record high zT value of 1.8 at 900 K in a single-phase high-entropy-stabilized (Pb/Sn)(Se/Te/S) material [8]. However, the high-entropy engineering approach has not been successfully applied in other classes of TE materials. One of the biggest challenges is phase separation within the phase matrix due to the presence of multiple elements. Consequently, electrons scatter across phase boundaries, diminishing the electronic transport of HEAs and limiting their TE performance. Thus, maintaining electrical conductivity through single-phase stabilization is crucial for achieving high zT in high-entropy TE materials. The core effects of high-entropy materials are closely tied to transport properties, aiming to enhance band degeneracy, create multi-scale microstructures, reduce κ_L, and introduce a synergistic effect, thereby accelerating the development of thermoelectrics (Figure 1c).

In this review, we present the recent developments, strategies, challenges, and future perspectives in high-entropy engineered TE materials. First, we depict the fundamental understanding of entropy engineering effects that can potentially lead to the advancement of TE performance. Second, we summarize the performance of high-entropy engineered TE materials explicitly in terms of phase stabilization, electrical transport properties, and

thermal conductivity. Third, we discuss the robust mechanical properties of TE materials, including hardness, elastic modulus, and fracture toughness, to reveal the longevity of TE devices. Fourth, we confer the deployment of an advanced computational design approach in high-entropy TE materials adopting ab initio, calculation of phase diagrams (CALPHAD), and data-driven methods. In conclusion, the review highlights the challenges and future perspectives for the advancement of high-entropy engineered TE performance.

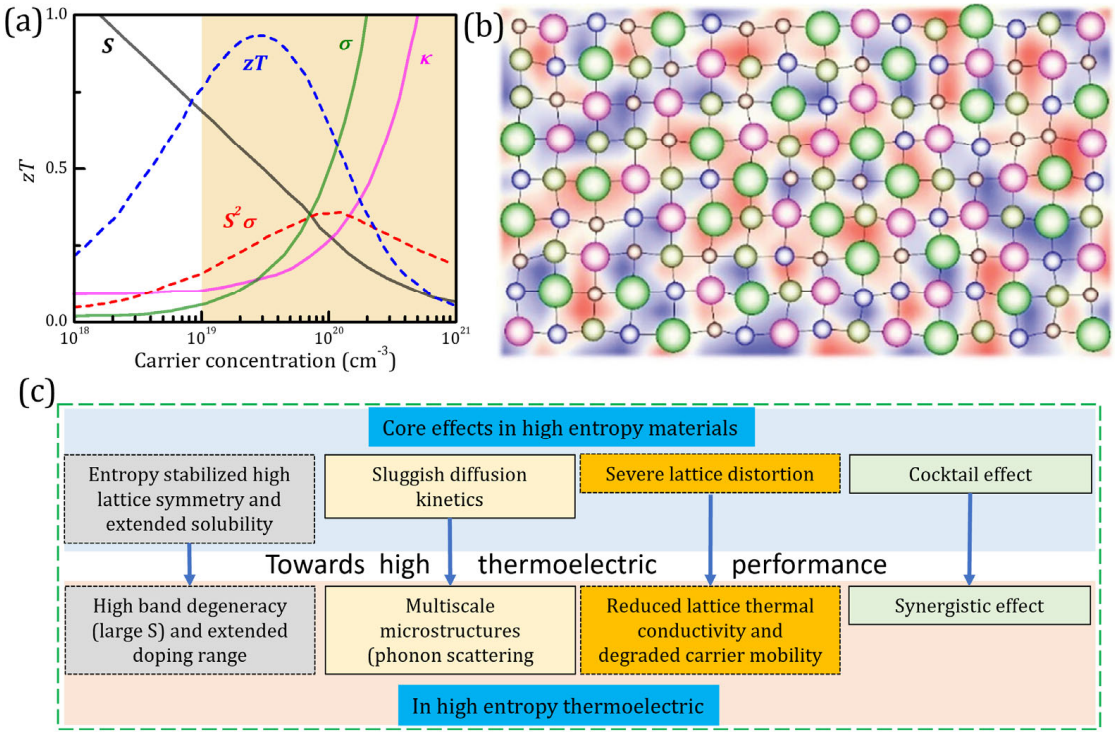

Figure 1. (**a**) Carrier concentration-dependent TE parameters. Reproduced with permission from [22]. Copyright (2008) Springer Nature. (**b**) Schematic of lattice distortion generated in the short-range order of a high-entropy material. Reproduced with permission from [28]. Copyright (2023) Wiley-VCH. (**c**) Core effects of HEAs.

2. Understanding Entropy Engineering in TE Materials

Entropy plays a crucial role in optimizing TE parameters, influencing charge carrier mobility (μ), κ, and thus TE performance. Mixing together several individual elements results in the reduction of Gibbs energy (ΔG_{mix}) through modifications in enthalpy (ΔH_{mix}) and enhancement in the entropy (ΔS_{mix}) of a system according to Gibb's phase rule, $\Delta G_{mix} = \Delta H_{mix} - T\Delta S_{mix}$. In some instances, $T\Delta S_{mix}$ can balance ΔH_{mix} and drive ΔG_{mix} to become more negative. The interplay between ΔH_{mix} (typically positive) and $-T\Delta S_{mix}$ (usually negative) can lead to "entropy stabilization". Entropy stabilization is a phenomenon in which a single-phase structure dominates at elevated temperatures, while a multiphase material prevails at lower temperatures. Entropy stabilization can only be observed when entropy becomes the primary force in the thermodynamic landscape and influences structure and phase behavior [29]. By studying the delicate balance between ΔH_{mix} and $-T\Delta S_{mix}$, we can better understand the structural and thermodynamic properties of these HEAs. The change in enthalpy (ΔH) can be expressed as $\Delta H = \Delta H_s + \Delta H_c$ [30], where ΔH_s is the enthalpy change due to internal strain energy resulting from the usage of different elements with varying atomic size and mass, and ΔH_c denotes the enthalpy change due to internal ionic field energy arising from the redistribution of the electron cloud. The major contribution of ΔH comes from ΔH_s, which is determined by the shear modulus, atomic radius, and atomic mass mismatch of the alloying elements [30]. The entropy of a given system refers to its number of possible microscopic configurations. The

greater the microscopic configurations, the greater the phonon disorder and scattering effect. Moreover, high ΔS_{conf} in materials is associated with several important features, such as cocktail effects, local lattice distortions, high defect density, and improved stability of the crystal structure [31]. This approach offers a wide range of opportunities to customize properties to fit specific applications, making HEAs an extremely attractive option for TE materials. The benefits and effectiveness of high ΔS_{conf} with respect to TE properties are summarized in Figure 1c, which will be detailed as follows.

2.1. Lattice Distortion

When atoms or ions of varying sizes, valences, or electronegativities coexist in the same sublattice, they introduce strain/distortion in the lattice, which can significantly impact the properties of materials. These distortions depend on the discrepancy in atomic and/or ionic radii, and through local atom and/or ion displacements, the Madelung constant governs the electrostatic potential of a crystal. For example, based on the Gruneisen parameter, γ, Fultz observed that even a minor modification of 1% in interatomic spacing can result in a significant change of approximately 12% in interatomic forces, while a 10% change can lead to a complete breakdown of the crystal structure [32]. These distortions largely affect the defect concentration and its impact on properties as well.

2.2. Structural Stabilization

Entropy stabilization is one way to achieve structural stabilization, which is essential in phase transitions. In binary materials, stabilization effects beyond the solubility threshold have been observed, resulting in the emergence of stable structural types that are not typically present under normal conditions. The origins of these effects are multifaceted and influenced by a variety of factors that collectively contribute to structural stabilization.

2.3. Cocktail Effect

The cocktail effect is observed when a combination of different elements or materials displays unique properties that cannot be traced back to any individual component. The interactions between the small units that make up the mixture give rise to the unpredictable properties of the whole system. Altering the composition or stoichiometry of a hybrid material can result in significant changes in its properties due to modifications in the interactions between the components [33]. This opens new avenues for tailoring material properties by selecting specific elements and modifying the stoichiometry.

Tailoring HEAs for specific applications is feasible due to their ability to control composition and defect structure. Changes in mechanical, electronic, and electrochemical properties depend on the composition. HEAs exhibit complexity, with increased defect density contributing to their intricacy. Disorder in HEAs directly impacts κ. Increased disorder and lattice distortions disrupt regular phonon vibrations, which are primarily responsible for heat conduction, by introducing phonon scattering centers. Simultaneously, an increase in ΔS_{conf} can enhance solubility limits and reduce electron scattering processes by eliminating phase boundaries in systems that would otherwise form multiple phases, thereby improving σ. High-entropy engineering enables the coupling of high σ with low κ, a prerequisite for high-performance TE [34]. Moreover, each term such as κ_L, μ_H, S, σ, and m^* can be tuned in different ways to obtain the maximum zT. Therefore, meaningful comparison of zT among different materials is possible only when the alloys/compounds are confirmed to be optimally doped [35]. Table 1 summarizes the effects of entropy engineering on various TE properties.

Table 1. Influence of entropy engineering on various TE properties.

Factors	Advantages of Materials	Entropy Engineering Effects
Composition	The compositional variation affects ΔS_{conf} and extends solid solubility	Structural stabilization and cocktail effect
	Access to increased composition space in a multicomponent domain	Structural stabilization due to ΔS_{conf}
Electrical	Changes in band structure and defect density, high electrical conductivity	ΔS_{conf}, lattice distorsion, cocktail effect
Thermal	Lower thermal conductivity	Lattice distortion induced phonon scattering
Mechanical	Distortion modified defect interaction	Lattice distortion, cocktail effect

3. Entropy Engineering to Enhance Materials' *zT*

Although high-entropy engineered TE materials often reveal the reduction of carrier mobility owing to the enhanced electron scattering, it can facilitate high S and low κ leading to high zT (Table 2). In the past few years, a high-entropy engineering strategy has been utilized in various TE materials exhibiting great potential to advance significant zT performance (Table 2 and Figure 2). Among them, chalcogenides exhibit superior TE performance through high-entropy design. For instance, a high peak zT of 2.0 at 900 K is obtained in a high-entropy PbSe-based material through a manipulated hierarchical structure by increasing ΔS_{conf} [9]. Jiang et al. reported that high-entropy-stabilized single-phase $Pb_{0.89}Sb_{0.012}Sn_{0.1}Se_{0.5}Te_{0.25}S_{0.25}$ material, with a high zT of 1.8 at 900 K, provides an avenue to improve TE performance for high-entropy engineered TE materials [8]. The same research group further realized both a superior zT of 2.7 at 750 K and high PF in a high-entropy $Ge_{0.61}Ag_{0.11}Sb_{0.13}Pb_{0.12}Bi_{0.01}Te$ TE material due to band convergence by increasing crystal symmetry; subsequently, they demonstrated the coexistence of low κ and high PF in the high-entropy GeTe-based material [10]. Moreover, $Ge_{0.84}In_{0.01}Pb_{0.1}Sb_{0.05}Te_{0.997}I_{0.003}$ shows a remarkable zT of 2.1 at 800 K due to band convergence induced by the high-entropy design [36]. Ma et al. reported $AgMnSn_{0.25}Pb_{0.75}SbTe_4$, a p-type semiconductor crystallized in a rock-salt structure, with a peak zT of 1.3 at 773 K and an average zT value of $_{0.8}$ in the temperature range of 400–773 K due to effective band convergence and high density-of-states effective mass [37]. They proposed that the increase in lattice distortion degree is important to achieve low κ, and thus the TE performance for HEAs. Recently, Gao et al. demonstrated the role of an adaptable sublattice in stabilizing HEAs and achieved a peak zT of 1.3 at 700 K in $Mg_{2-\delta}Si_{0.12}Ge_{0.13}Sn_{0.73}Bi_{0.02}$, which is competitive among the best values reported in Mg_2X-based materials [38].

It is worth noting that besides the high zT value of a suitable TE material, a high PF is desired considering the output power performance. In this context, half-Heusler (hH) materials are promising for mid-temperature to high-temperature TE materials as they exhibit a large PF, excellent mechanical properties, and good thermal stability [17]. However, the TE performance of the hH alloys is limited due to their intrinsically high κ_L ~10 W/m-K for stoichiometric compounds. For example, a low zT of $_{0.2}5$ is achieved in a high-entropy $MFe_{0.6}Co_{0.4}Sb$ hH alloy [11]. The maximum zT of $_{0.8}8$ at 873 K has been reported in a high-entropy engineered $Nb_{1-x}M_xFeSb$ (M = Ti, V, Hf, Mo, or Zr with an equimolar ratio) hH material [12]. Although a significant reduction in κ is realized through high-entropy design, the electrical transport properties are also significantly affected due to phase segregation [11,12]. As a result, the zT value of high-entropy hH alloys is still limited to less than 1.0. Therefore, in the design of HEAs, single-phase stabilization is one of the most crucial factors in optimizing the TE performance of any class of materials.

Table 2. High-entropy engineered TE materials with zT_{max}, *PF*, and κ at zT-peak temperature in chronological order.

Year	High-Entropy TE Materials	PF ($\mu Wcm^{-1}K^{-1}$)	κ ($Wm^{-1}K^{-1}$)	zT_{max}	zT^{peak} (K)	Ref.
2016	$(BiSbTe_{1.5}Se_{1.5})_{1-x}Ag_x$ [x = 0.9%]	6.5	0.43	0.63	450	[39]
2017	$Pb_{0.94}SnTeSeLa_{0.06}$	12.6	1.37	0.8	873	[40]
2018	$(Sn_{0.74}Ge_{0.2}Pb_{0.1})_{0.75}Mn_{0.275}Te$	17.9	1.13	1.42	900	[41]
2018	$Nb_{0.8}M_{0.2}FeSb$ (M = Hf, Zr, Mo, V, Ti; equimolar)	42.2	4.19	0.88	873	[12]
2018	$Ag_9GaSe_{5.53}Te_{0.45}$	6.7	0.35	1.6	850	[42]
2019	$Ti_2NiCoSnSb$	5.7	10.5	0.047	860	[43]
2019	$Ge_{0.84}In_{0.01}Pb_{0.1}Sb_{0.05}Te_{0.997}I_{0.003}$	30.6	1.19	2.1	800	[36]
2020	$AgSnSbSe_{1.5}Te_{1.5}$	9.8	0.62	1.14	723	[44]
2020	$Ag_{0.25}Pb_{0.5}Bi_{0.25}S_{0.4}Se_{0.5}Te_{0.1}$	4.6	0.61	0.54	723	[45]
2021	$Ga_{0.025}(Sn_{0.25}Pb_{0.25}Mn_{0.25}Ge_{0.25})_{0.975}Te$	18.5	1	1.52	823	[46]
2021	$AgMnGeSbTe_4$-1 mol% Ag_8GeTe_6	13.9	0.85	1.27	773	[47]
2021	$Cu_{0.8}Ag_{0.2}(ZnGe)_{0.1}(GaIn)_{0.4}Te_2$	6	0.48	1.02	820	[48]
2021	$Pb_{0.935}Na_{0.025}Cd_{0.04}Se_{0.5}S_{0.25}Te_{0.25}$	16.2	0.73	2	900	[9]
2021	$Pb_{0.89}Sb_{0.012}Sn_{0.1}Se_{0.5}Te_{0.25}S_{0.25}$	12.5	0.63	1.8	900	[8]
2022	$Ge_{0.61}Ag_{0.11}Sb_{0.13}Pb_{0.12}Bi_{0.01}Te$	28.6	0.834	2.7	750	[10]
2022	$MFe_{0.7}Co_{0.3}Sb$ (M = equimolar Ti, Zr, Hf, V, Nb, Ta)	7.8	2.88	0.25	923	[11]
2022	$AgMnSn_{0.25}Pb_{0.75}SbTe_4$	11.3	0.67	1.3	773	[37]
2022	$Cd_{0.02}(Sn_{0.59}Pb_{0.15}Ge_{0.2}Sb_{0.06})_{0.98}Te$	19.1	1.02	1.5	800	[18]
2022	$Cu_{1\cdot87}Ag_{0.13}(In_{0.06}Sn_{0.94})Se_2S$	4.35	$_{0.2}5$	1.52	873	[49]
2022	$Ge_{0.82}Sb_{0.08}Te_{0.9}(MnZnCdTe_3)_{0.1}$	17.2	1	1.24	723	[50]
2023	$Mg_{2-\delta}Si_{0.12}Ge_{0.13}Sn_{0.73}Bi_{0.02}$	40	2.15	1.3	700	[18]
2023	$Pb_{0.9}Na_{0.04}Mn_{0.06}Te_{0.9}S_{0.05}Se_{0.05}$	22.1	$_{0.8}7$	2.1	825	[51]

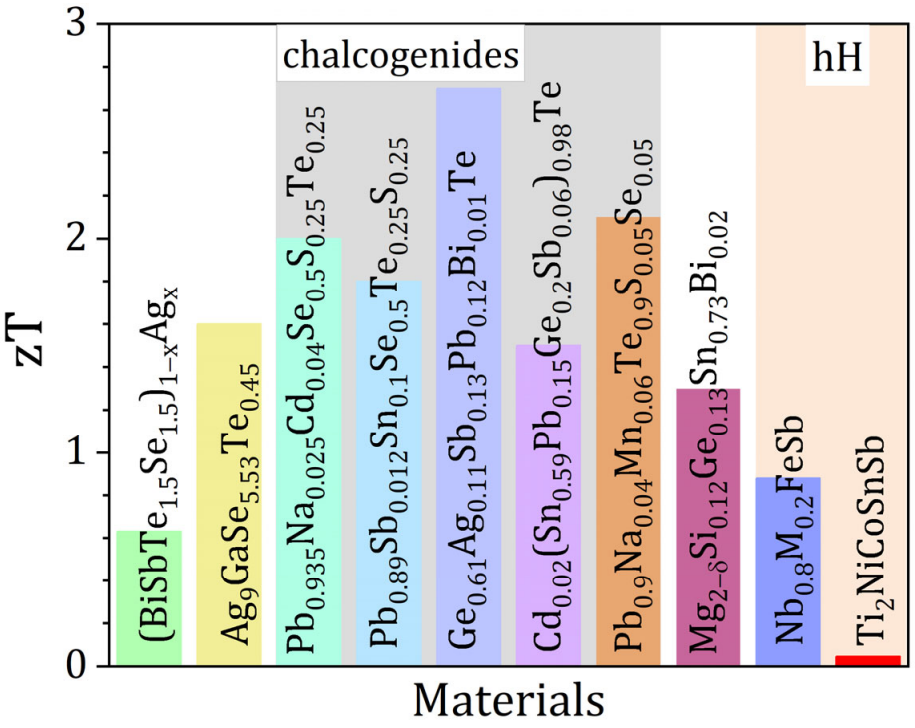

Figure 2. The state-of-the-art zT of high-entropy engineered materials. Data taken from the references [8–10,12,19,38,39,42,43,51].

3.1. Phase Stabilization

High-entropy engineering imparts a driving force to form high-entropy-stabilized materials through the reduction of Gibbs free energy. The crystal phase of HEAs stabilizes at elevated temperature according to the Gibbs phase rule. ΔS of HEAs can dominate the H of

a system, which consequently leads to $\Delta G < 0$. As a result, single-phase HEAs are obtained through high-entropy-driven structural stabilization (Figure 3a) [8]. It is noteworthy that HEAs surpass the maximum solubility of conventional low-entropy alloys. In TE materials, few successful studies have been reported so far, where the enhancement of entropy toward the high-entropy region successfully stabilizes the single phase. For example, an increase in ΔS_{conf} by the alloying of Sn assists in stabilizing the single cubic phase of n-type high-entropy (Pb/Sn) (Se/Te/S) materials over the solubility limit, which was observed to exhibit several splitting peaks in the (200) peak and associated with multiple phases [8]. This is attributed to the entropy-driven structural stabilization effect, providing a positive effect of high entropy strategy. This has been further realized to improve structural symmetry. For example, a high-entropy GeTe-based material, $Ge_{0.84}In_{0.01}Pb_{0.1}Sb_{0.05}Te_{0.997}I_{0.003}$, demonstrated the single phase of the GeTe phase with a rhombohedral structure without any traces of impurities [36]. Moreover, the stability of the high-temperature cubic phase has been realized with an increase in ΔS_{conf}, which shifts the phase transition temperature from rhombohedral to cubic structure to a lower temperature (Figure 3b) [36]. This indicates an enhancement in crystal structural symmetry, which can be correlated with the increase in the interaxial angle (Figure 3c) [36]. However, the solubility of potential high-temperature hH TE materials through high entropy engineering has not been successfully explored [11] and requires further attention from the TE community.

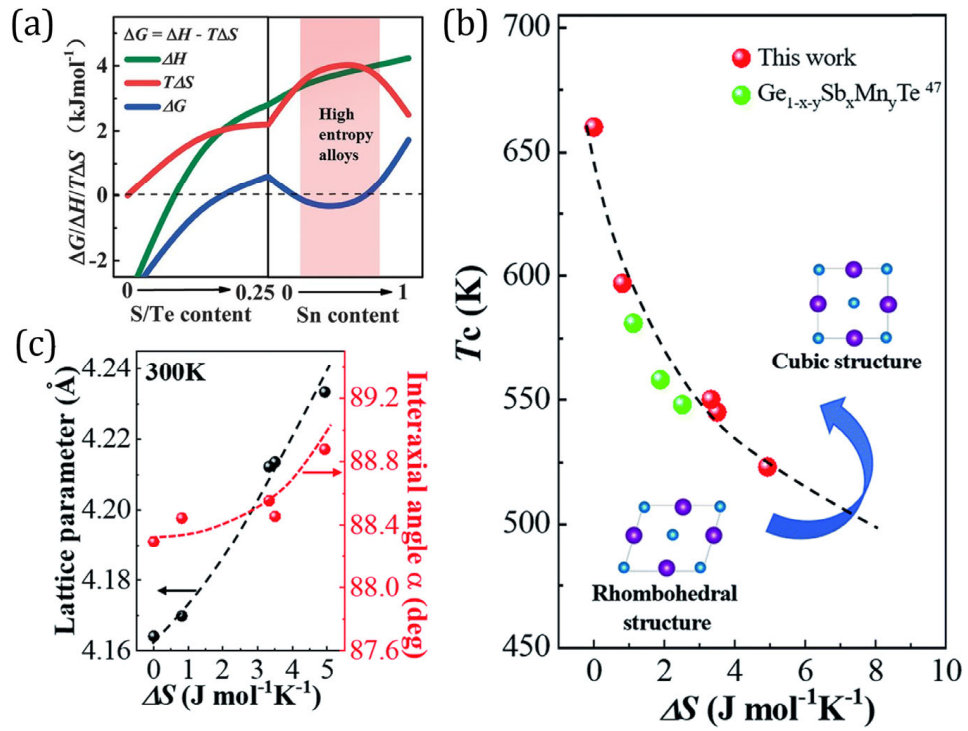

Figure 3. (**a**) The calculated *S*, *H*, and *G* as a function of S/Te and Sn content in high-entropy engineered $Pb_{0.99-y}Sb_{0.012}Sn_ySe_{1-2x}Te_xS_x$ alloy, demonstrating structural stabilization through minimization of ΔG. Reproduced with permission from [8]. Copyright (2021) AAAS. (**b**) Structural phase transition temperature of GeTe-based alloy shifts towards low temperature with an increase in entropy (ΔS): entropy-driven crystal symmetry of high-entropy alloy. Reproduced with permission from [36]. Copyright (2019) Royal Society of Chemistry. (**c**) Enhancement of interaxial angle with an increase in ΔS indicating the enhancement of crystal structural symmetry. Reproduced with permission from [36]. Copyright (2019) Royal Society of Chemistry.

3.2. Optimization of Power Factor

Enhancement in the chemical complexity of multiple elements with various atomic sizes and masses often results in phase segregation in the phase matrix. Therefore, the

electron transport in high-entropy TE materials is hindered due to induced enhanced electron scattering across the phase boundary, leading to degradation in μ_H. High-entropy engineering with adaptable sublattices facilitates band convergence, which can enhance S and compensate for σ to maintain a high PF. In this context, the optimization of PF is required to enhance zT, as well as for the power output from the device. Through Cd, Se, and S alloying in PbSe-based material [9], the valence band maximum was pushed down, while the conduction band minimum was pushed up simultaneously, leading to a decreased energy difference ($\Delta E_{L-\Sigma}$) between the light (L) and heavy (Σ) valence bands (Figure 4a,b). Therefore, the valley degeneracy N_v is largely increased, resulting in enhanced S and PF. Jiang et al. demonstrated that high-entropy engineering in the GeTe-based material $Ge_{0.61}Ag_{0.11}Sb_{0.13}Pb_{0.12}Bi_{0.01}Te$ increases the crystal structure symmetry, which leads to unusual delocalization of electron distribution in the distorted rhombohedral structure. This results in band convergence, which maintains superior electrical properties [3]. Similarly, co-alloying of (Sn, Ge, Pb, and Mn) in SnTe enhances band convergence and band effective mass, which enhances S even though carrier concentration increases, resulting in a high PF. However, high-entropy engineered hH materials have not been fruitful, despite low-entropy materials showing a high PF. The major obstacle in high-entropy hH alloys is severe electron scattering at the phase boundaries due to phase separation in the matrix, which reduces PF significantly. A comparison of the PF of different types of high-entropy engineered materials is shown in Figure 4c.

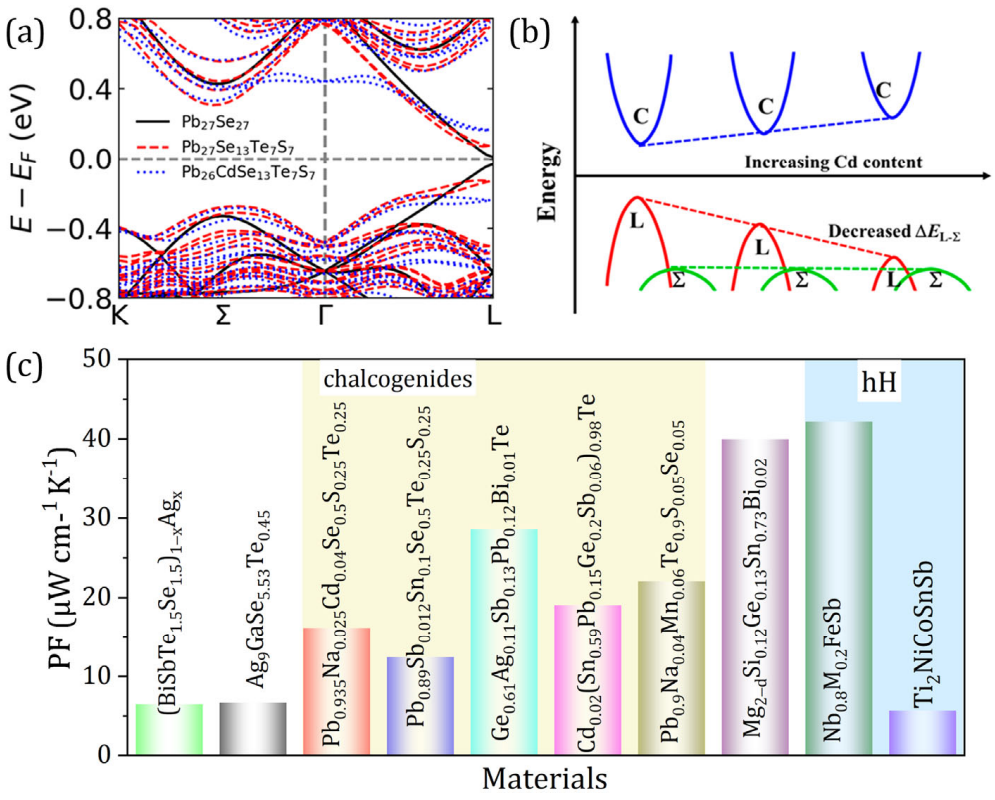

Figure 4. (**a**) Calculated band structures of PbSe-based high-entropy alloys. (**b**) Schematic diagram of band convergence by alloying Cd, Se, and S to PbSe. Reprinted with permission from [9]. Copyright (2021) Jiang et al. Distributed under the Creative Commons Attribution 4.0 License (**c**) A comparison of the PF of high-entropy engineered materials. Data taken from the references [8–10,12,18,38,39,42,43,51].

3.3. Low Thermal Conductivity

The doping of elements with different mass and size leads to strain field fluctuation and significantly suppresses κ_L. Due to the strain field fluctuations during isoelectronic

alloying in the sublattice, various pathways are created for point defect scattering in phonons. The resulting disorder scattering parameter (Γ_{cal}) can be calculated using the following equation [52]:

$$\Gamma_{cal} = \Gamma_{mass} + \Gamma_{size} \quad (3)$$

where Γ_{mass} and Γ_{size} are the contributions to the scattering factor due to the difference in the atomic mass and size of the elements, respectively. Γ_{size} depends on the size as well as the nature of bonding among various elements and the nature of the sublattice in which they are doped. If the contribution of Γ_{size} is negligible, $\Gamma_{cal} \approx \Gamma_{mass}$. In quaternary multicomponent alloys, a low κ_L is observed along the binaries with a high atomic mass difference. Alloying/doping elements with a large atomic mass mismatch and a small size mismatch is found to be beneficial in eliminating the effect of κ_L and μ_H. For example, in hH alloys, a large mass mismatch with a smaller size mismatch between group *V* and *VI* elements results in large thermal but small electronic perturbation. However, if elements with intermediate atomic and mass mismatch are doped, they can diminish the overall scattering effect. Thus, in HEAs, utmost care must be taken while deciding on factors such as what, how much, what order, and in which sublattice(s) to alloy [41,53,54]. Furthermore, the following approaches can be considered to suppress κ_L: (i) isoelectronic alloying on different sublattices; (ii) each element added/doped must introduce an independent and significant scattering mechanism that acts orthogonally; (iii) phase separation or precipitation in nano scale due to the strain resulting from atomic size mismatch; (iv) defect generation such as vacancies, dislocations, and stacking faults; (v) increasing the grain boundaries by refining the grain size; (vi) developing hierarchical microstructure along with the formation of secondary phases; (vii) generating incoherent phase interfaces, which can increase both Γ_{mass}.

The chemical complexity of the elements in HEAs leads to severe lattice distortion in the short-range order of the high-entropy phase. Consequently, it scatters the heat-carrying phonons and the κ_L of the material reduces significantly due to strong high-frequency phonon scattering, posing a potential avenue for achieving high zT values. The very suppressed κ_L from the atomic-scale phonon mean-free path is the key feature of HEAs. For example, the manipulation of hierarchical structure through high-entropy engineering provides a difference scale of lattice defects, including point defects, planar defects, nanoprecipitates, and mesoscopic precipitates, which become the scattering sources for low- to high-frequency phonons, leading to a significantly suppressed κ_L in $Pb_{0.935}Na_{0.025}Cd_{0.04}Se_{0.5}S_{0.25}Te_{0.25}$ alloy (Figure 5a) [9]. Because of the hierarchical structure design with high entropy in PbSe material, the realized κ_L (~0.33 $Wm^{-1}K^{-1}$) approaches the theoretical minimum (~0.31 $Wm^{-1}K^{-1}$, calculated based on the Cahill model) [10]. High-entropy design in $Ge_{0.61}Ag_{0.11}Sb_{0.13}Pb_{0.12}Bi_{0.01}Te$ alloy demonstrated an ultralow κ_L (~0.3 $Wm^{-1}K^{-1}$) due to the localized phonons' behavior, induced by the entropy-driven disorder generated in the lattice, which extensively hampered the propagation of transverse phonons and increased anharmonicity [10]. Moreover, an ultralow κ (~0.44 $Wm^{-1}K^{-1}$ at 873 K) is realized in high-entropy chalcogenide $Cu_{1.87}Ag_{0.13}(In_{0.06}Sn_{0.94})Se_2S$ nanocrystals through the design of a metastable cubic phase induced by size-driven structural stabilization (Figure 5b) [49]. The high-entropy approach has also been successful in ceramic TE. Maity et al. demonstrated that multicomponent doping in an equimolar ratio in the B-site of perovskite material (ABO_3) can help reduce κ (0.7 $Wm^{-1}K^{-1}$ at 1050 K) in $Sr(Ti_{0.2}Fe_{0.2}Mo_{0.2}Nb_{0.2}Cr_{0.2})O_3$ high-entropy ceramic due to enhanced multi-phonon scattering [55]. In $Ca_{0.2}Sr_{0.2}Ba_{0.2}Pb_{0.2}La_{0.2}TiO_3$ high-entropy ceramic, Zheng et al. observed a minimum κ of 1.17 $Wm^{-1}K^{-1}$ at 923 K due to the large lattice distortion and huge mass fluctuation effect [56].

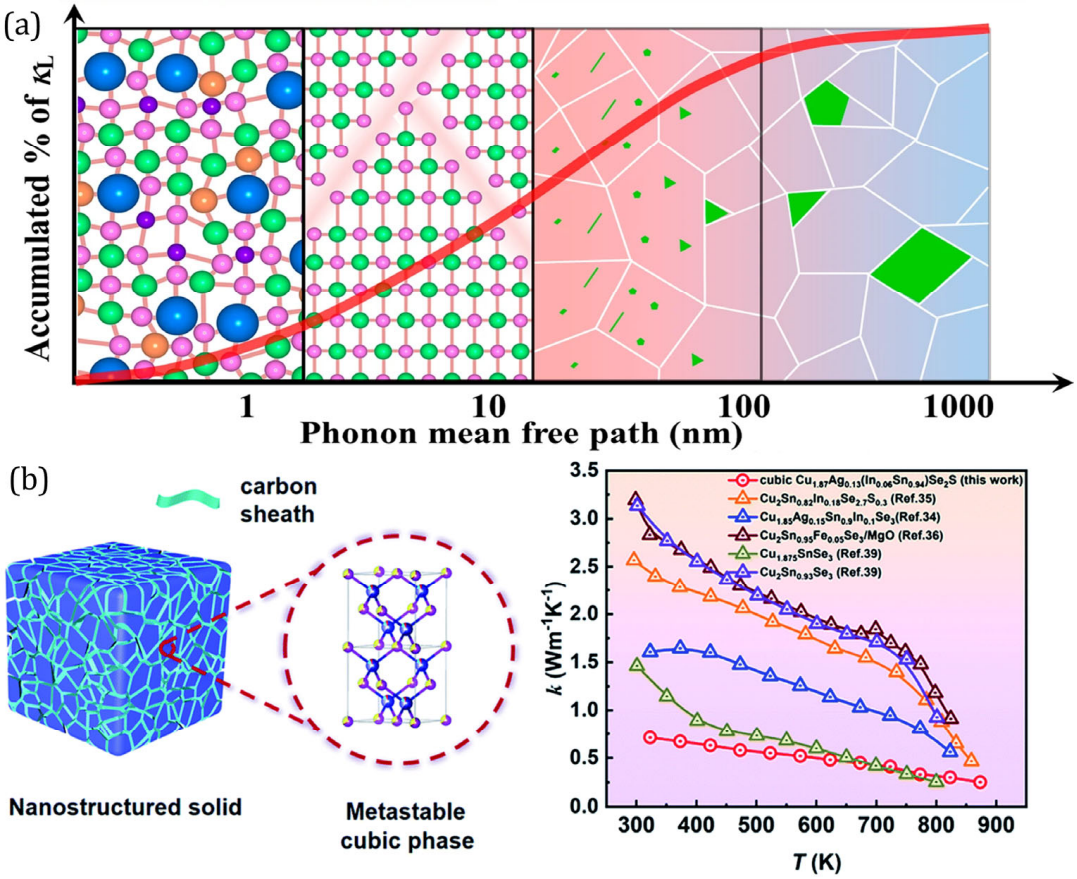

Figure 5. (**a**) Schematic diagram of all-scale hierarchical structures (point defects, planar defects, nanoprecipitates, and mesoscopic precipitates) and accumulated lattice thermal conductivity (the red line) as a function of the phonon mean free path. Reproduced with permission from [9]. Copyright Jiang et al. Distributed under the Creative Commons Attribution 4.0 License. (**b**) Metastable cubic phase stabilized in high-entropy $Cu_{2-y}Ag_y(In_xSn_{1-x})Se_2S$ nanostructured solids (left), which demonstrated low thermal conductivity (right). Reproduced with permission from [49]. Copyright (2022) Royal Society of Chemistry.

4. Robust Mechanical Properties

For practical application considerations, TE materials and devices must be mechanically robust and resist cracking or failure from vibrations. TE devices are utilized in various applications, including space exploration, industrial waste heat recovery, and wearable self-powered equipment. However, to be commercially viable, these devices require exceptional thermal stability and mechanical properties to prevent the element from becoming volatile and the interface from becoming diffused [57]. Mechanical properties play a crucial role in determining their lifespan, making them a highly sought-after technology. Conventional TE alloys' mechanical properties have been extensively studied and documented in the literature [57–62].

4.1. Materials' Mechanical Properties

There are various techniques available for measuring the hardness of a material, including macro-, micro-, and nanoindentation methods. By analyzing these measurements, it is possible to calculate both the hardness and elastic modulus of the material. Poisson's ratio must be known to determine the elastic modulus accurately. When assessing the mechanical properties of TE materials, it is of utmost importance to consider a variety of factors, including the synthesis route, compositional variations, surface roughness (sample preparation), sample density, nature of testing, and loading conditions. These elements can

significantly influence the ultimate value of the mechanical properties of TE materials [63]. Hence, it is crucial to meticulously consider these factors to attain accurate and reliable results in the assessment of the mechanical properties of TE materials. The mechanical properties of high-entropy TE materials are critical but have rarely been reported so far. We will mainly focus on various levels of mechanical performance based on conventional TE materials, which can further guide the mechanical considerations in high-entropy TE materials in the future.

4.1.1. Hardness (H)

For hH materials such as TiNiSn, ZrNiSn, and HfNiSn, the cast samples exhibited higher hardness (>10 GPa) than their ball-milled and sintered counterparts. The study by Verges et al. showed that the substitution of Ti by Zr or Hf in any higher-order system resulted in reduced hardness. The samples with densification aids showed slightly higher values than those without the aids [64]. The influence of composition on p-type and n-type hH alloys has been studied extensively by Verges et al. and O'Connor et al. [65,66]. A substantial increase in hardness has been reported with Ni inclusions for both hH and Skutterudites. The hardness values were strongly dependent on the density of the samples, rather than on the loads used. Fan et al. established an exponential relationship between hardness and porosity, which was confirmed by $Ti_{0.75}Hf_{0.75}NiSn$ (n-type) and $TiFe_xCo_ySb$ (p-type) alloys [66]. From the literature data, it can be concluded that the hardness values do not differ much for n-type and p-type HH alloys [67].

4.1.2. Elastic Modulus

The elastic modulus is important as it affects the fracture strength and thermal shock resistance. Young's modulus (E) is sensitive to measurement techniques. Values of nanoindentation represent local behavior, and hence more data points are required to account for a bulk response. Generally, resonant ultrasound spectroscopy is used to obtain a bulk response. These values are always found to be lower than the indentation values, due to the overplay of local composition fluctuations in the latter. A concise review of the nanoindentation data of various TE alloys is summarized by He et al. [59]. For example, in hH alloys, the following results were observed: (i) E and H decrease with increasing Co and decreasing Fe; (ii) E increases with Sn addition; (iii) Substitutions of Ir, Rh, and Pd on the Co or Ni site affect E. To understand the inherent nature of TE alloys, the ratio of bulk to shear modulus (B/G) was calculated according to Pugh's criteria. Rogl et al. found that the values lie in the range of $1.43 < B/G < 1.86$, indicating the brittleness of these TE alloys [61,67]. Moreover, it was observed that all TE alloys (hH, Skutterudites, Bi_2Te_3) obey the $\frac{H^3}{E^2}$ relation as shown in Figure 6. With this relation, it becomes easier to predict H through E and vice versa. On overall comparison, hH alloys have higher hardness and elastic modulus than other TE alloys, which agrees with the study by He et al. [59].

4.1.3. Indentation Fracture Toughness

According to Antis et al., indentation fracture toughness (K_{1c}) is given by the following equation:

$$K_{1c} = 0.016 \left(\frac{E}{H}\right)^{0.5} \left(\frac{P}{c^{1.5}}\right) \quad (4)$$

where E is the elastic modulus (GPa), H is hardness (GPa), P is the indentation load (N), and c is the crack length (m). According to Figure 6, hH alloys exhibit higher E and H values, indicating higher fracture toughness values as well. The K_{1c} values for $Ti_{1-x}Zr_xNiSn$ and $Ti_{1-x}Hf_xNiSn$ hH alloys were found to increase with increasing Zr/Hf concentrations [65].

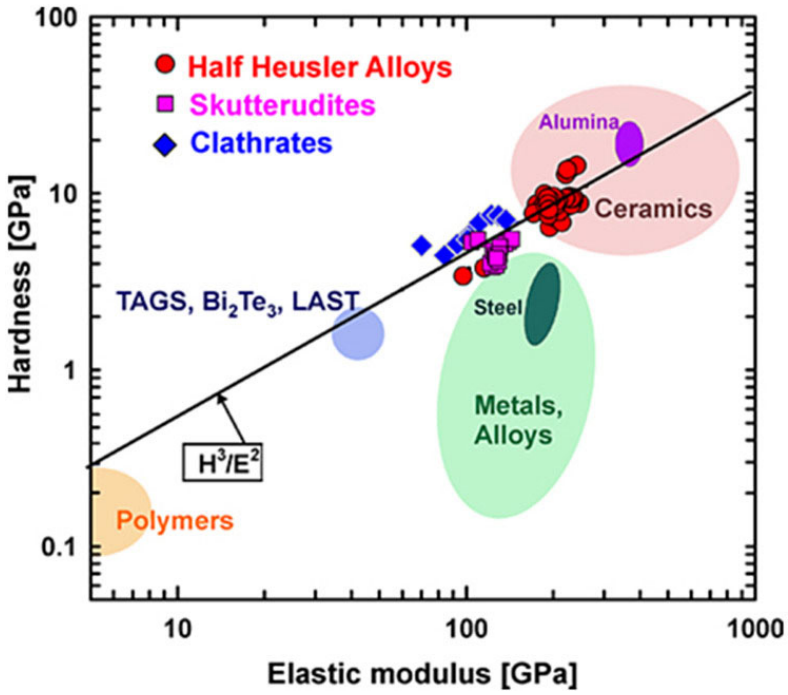

Figure 6. A plot of hardness vs. modulus of various TE alloys in comparison to other materials. Reprinted with permission from [67]. Copyright (2017) Elsevier.

4.1.4. Mechanical Response at High Temperatures—Compressive Strength, Creep

In the case of TEGs, bulk devices in particular encounter a certain degree of external pressure during operation. The peak compressive strength that these TE materials can endure is crucial for the reliable performance and lifetime of devices. Moreover, the effect of temperature on these properties has been less explored in the literature. Rogl et al. and Jung et al. studied the effect of temperature on the elastic modulus and thermal expansion coefficients for hH alloys [67,68]. The studies revealed that the elastic modulus exhibited an inverse relation, whereas the thermal expansion coefficients showed a direct relation with increasing temperature. In the literature, high-temperature mechanical data of HEA TE materials are very scarce. Moreover, the studies are focused on hH alloys because of their high hardness, elastic modulus, TE performance, and phase purity. All of these factors play a major role in the deformation or failure mechanism. High-temperature compression behavior of $Zr_{0.5}Hf_{0.5}NiSn_{0.985}Sb_{0.015}$ HH alloy was studied by Lu et al. in the temperature range of 300–1100 K [69]. The range of typical hardness and elastic modulus for different types of thermoelectric materials is shown in Figure 6. The alloy was prepared through induction melting, followed by pulverization and consolidation through hot pressing. With an increase in temperature, the elastic modulus and compressive strength decreased owing to the grain boundary weakening, which made a pathway for aggressive oxidation and segregation of alloying elements, as shown in Figure 7. The compressive strength of the alloy decreased to ~214 MPa at 1100 K from ~785 MPa at 300 K.

The creep behavior and pre- and post-creep thermoelectric performance of $Hf_{0.3}Zr_{0.7}NiSn_{0.98}Sb_{0.02}$ alloy was studied recently by Malki et al. [70]. The hH alloy exhibited finer grain sizes (~1–7 mm) and could withstand a compressive strength of ~360 MPa for 23 days at 873 K. The sample that crept up to 46 MPa revealed better TE performance than the sample that crept to 360 MPa. The creep behavior of the hH alloy compared with other TE materials is shown in Figure 8.

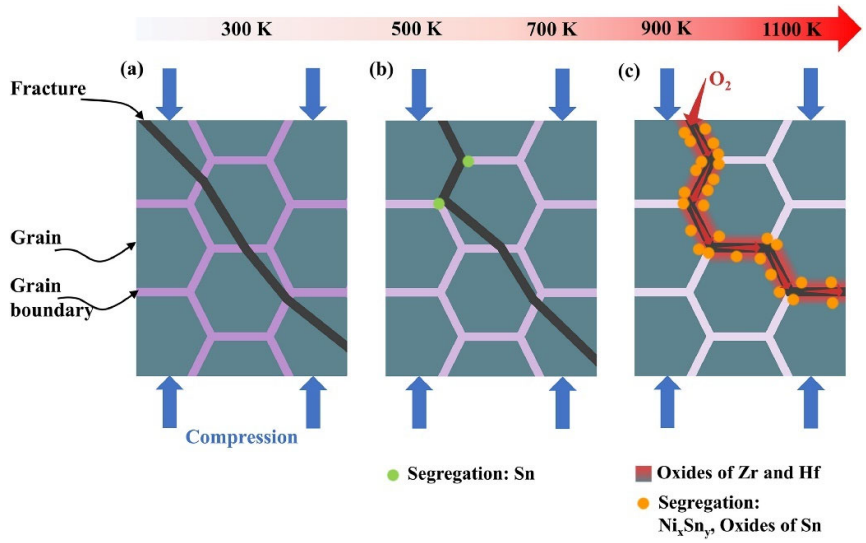

Figure 7. Schematic diagram of the compression fracture mechanism of $Zr_{0.5}Hf_{0.5}NiSn_{0.985}Sb_{0.015}$ at different temperatures: (**a**) room temperature (300 K), (**b**) medium temperatures (500 and 700 K), and (**c**) high temperatures (900 and 1100 K). Reprinted with permission from [69]. Copyright (2024) Elsevier.

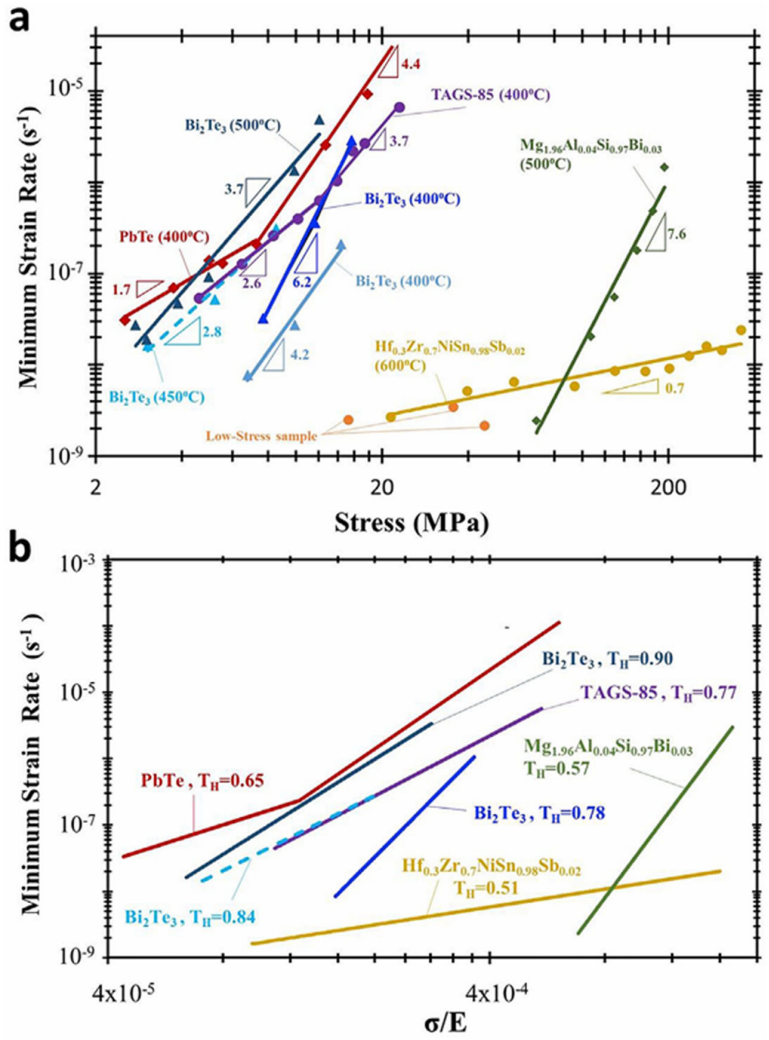

Figure 8. Double-logarithmic plots of minimum strain rate vs. (**a**) stress and (**b**) stiffness-compensated stress. The plot shows creep data of all TE alloys tested in the literature along with their homologous temperature. Reprinted with permission from [70]. Copyright (2019) Elsevier.

4.2. Mechanical Failure Modes of TE Devices

TEG usually encounters mechanical issues that can significantly reduce its output power and efficiency. Over time, various types of TEGs have been explored, including traditional bulk devices, inorganic thin-film devices, flexible organic devices, and flexible devices that utilize bulk thermoelectric legs [71]. Figure 9 presents an overview of the different types of TEGs and the potential mechanical failures they may face [57]. The failure of a TEG is primarily determined by the mechanical characteristics of the TE materials in use, which also dictate the device's mechanical properties. The quality of the connection between electrodes and materials is critical, and any mechanical damage to the electrodes or connections can result in decreased output performance or even complete TEG failure. Furthermore, the mechanical characteristics of the substrate can also affect a TEG's mechanical properties. Considering the possible failure mechanisms during service in Figure 9, fracture toughness, hardness, the elastic modulus, and compressive strength are important mechanical parameters to be understood for a robust TE device. The relevance of material hardness is not confined solely to its wear resistance but extends to its machinability, both of which are critical considerations for ensuring mechanical stability and efficient device manufacturing. The long-term durability of TE modules constructed from p- and n-type materials is significantly dependent on the matching of coefficients of thermal expansion of each leg-type material in the temperature range employed [72,73]. Hence, ensuring that these coefficients are well matched is a crucial aspect of optimizing the efficient and reliable operation of TE modules.

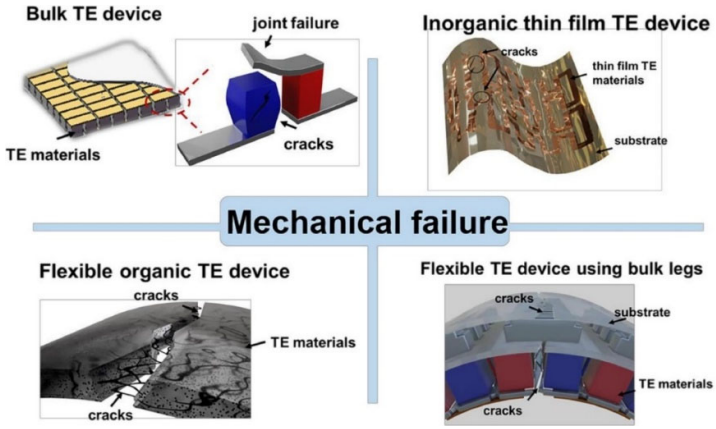

Figure 9. Schematic diagram of mechanical failure of various thermoelectric devices. Reprinted with permission from [57]. Copyright (2023) Elsevier.

5. Computational Design of Entropy-Engineered TE Materials

Efforts related to computation-driven rational design of materials have risen in popularity and importance in the recent past. Computational tools have become a reliable shortcut for the design of new alloys with superior properties because of the enhancement in the capabilities of computing resources. In contrast to experimental investigations with a trial-and-error approach involving high material costs and energy consumption, computational tools can serve as a guide to design materials efficiently by lessening the experimental trials. With a multitude of computational resources available for developing new materials, the approaches that are being employed commonly for the design of high-entropy thermoelectric materials can be conveniently divided into ab initio, CALPHAD (calculation of phase diagrams), and data-driven methods, as listed in Figure 10, which will be further elaborated in the following subsections.

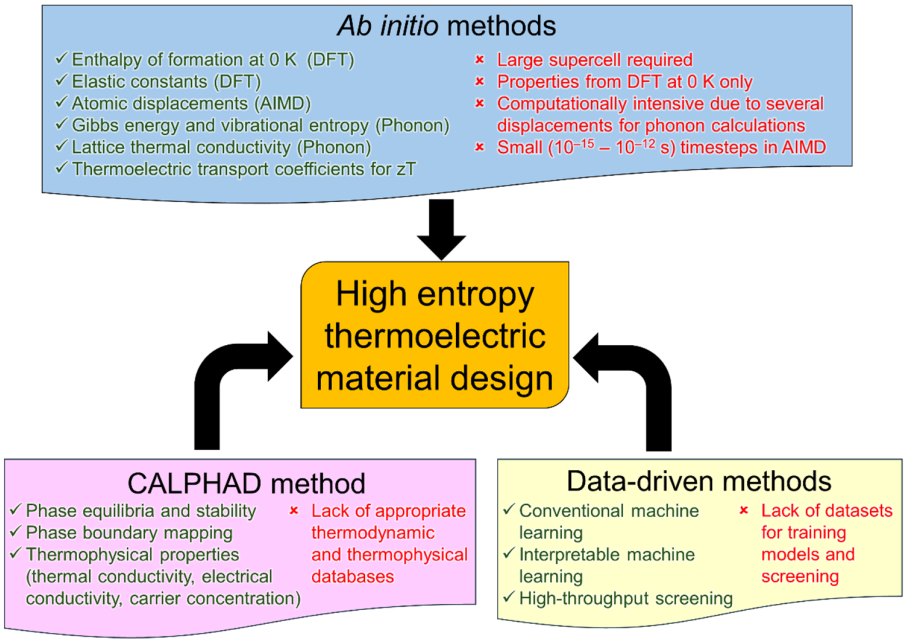

Figure 10. Classification of various computational tools that can be employed for the design of high-entropy TE materials, along with their limitations.

5.1. Ab Initio-Based Methods

Ab initio methods, which are also known as first-principles methods, have been extensively employed for the design and validation of high-entropy TE materials, mainly for (a) computing the enthalpy of formation and Gibbs energy of the material to understand the phase stability and (b) calculating the density of states. Ab initio methods are based on density functional theory (DFT), a quantum mechanical tool for computing the electronic structure of atoms and molecules and periodic/non-periodic solid phases. The DFT packages that are usually used for computing TE attributes are the Vienna Ab Initio Simulation Package (VASP) [74,75], which uses projector-augmented-wave formalism with frozen core approximation, and the Wien2K [76] package, which employs all-electron full-potential linearized augmented-plane wave formalism. It is worth noting that all the DFT calculations are implemented at a temperature of 0 K.

The enthalpy of formation (ΔH_{form}) of a compound can be calculated using DFT using the following equation:

$$\Delta H_{form}\left(A_xB_yC_z\right) = E_{total}\left(A_xB_yC_z\right) - xE_{total}(A) - yE_{total}(B) - zE_{total}(C) \quad (5)$$

where E_{total} is the total energy of each structure calculated using the DFT packages. The calculation of ΔH_{form} for periodic structures is straightforward, since atoms will occupy fixed positions. On the other hand, high-entropy materials necessitate the mixing of various components in one or more lattice sites of the crystal structure. This requires the generation of disordered structures and separate frameworks that are available to generate the same to serve as input for the DFT calculations. Special quasirandom structures (SQS) [77] are the most frequently used method for generating disordered structures due to their ease of implementation. The *mcsqs* code included in the Alloy Theoretic Automated Toolkit (ATAT) [78] is used for generating the SQS structures. Besides, there are techniques available such as Korringa–Kohn–Rostoker (KKR) coherent potential approximation [79] and virtual crystal approximation [80] for generating random alloys. The major drawback in generating random alloys with mixed lattice site occupancies for DFT calculations is the large number of atoms required in the supercell to mimic alloying behavior. As shown in

Figure 11a, to generate a structure with mixed occupancy of Pb and Sn in one lattice site along with Te and Se in another lattice site in an NaCl-type face-centered cubic structure, a supercell with 64 atoms is required for generating the SQS structure to perform DFT calculations for PbSnTeSe high-entropy thermoelectric material [81]. This makes DFT calculations computationally intensive and demands higher computing power. Figure 11b shows the enthalpy of formation of high-entropy thermoelectric materials ($Ti_2NiCoSnSb$ and $Ti_{1.5}NiCoSnSb$) and other related compounds using Equation (5) for the high-entropy and hH TE materials determined using DFT calculations [82].

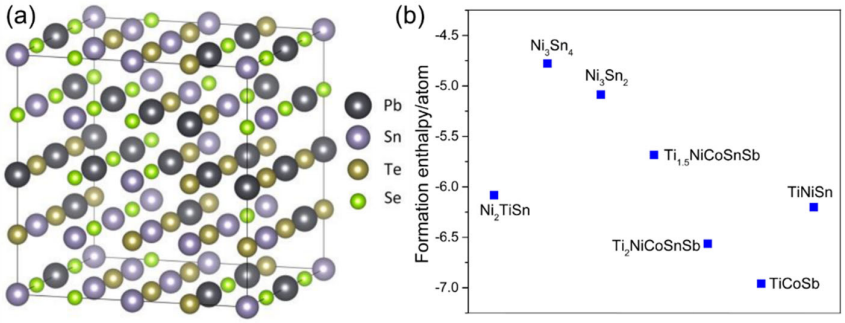

Figure 11. (**a**) Schematic of 64-atom supercell generated using a special quasirandom structure with the mixing of Pb and Sn atoms in one lattice site and the mixing of Se and Te atoms in the other lattice site in PbSnTeSe high-entropy thermoelectric material. Reprinted with permission from [81]. Copyright (2023) MDPI. (**b**) Enthalpy of formation of high-entropy thermoelectric and other related compounds for the high-entropy and half-Heusler thermoelectric materials calculated using density functional theory-based ab initio calculations. Reproduced with permission from [82]. Copyright (2023) Springer Nature.

Thermodynamic properties can be computed as a function of temperature using quasi-harmonic approximation (QHA) [83], which evaluates the volume dependence of phonon frequencies in a structure consisting of vibrating atoms. Since the volume dependence of phonon frequencies is considered, ΔG can be derived by calculating the volume and total energy as a function of temperature. The total entropy, ΔS, of HEA is a sum of ΔS_{conf} and ΔS_{vib} entropies. ΔS_{conf} can be estimated using the well-known Boltzmann equation. ΔS_{vib} can be computed using QHA as implemented by Phonopy code [84]. It is a Python-based open-source code for performing phonon calculations using the direct-force method for a supercell, an expanded unit cell of a material. The Gibbs energy calculated using Phonopy can be used to understand the stability of a high-entropy TE material as a function of temperature. In Figure 3a, the calculated configurational (calculated using Equation (1)), vibrational (calculated using Phonopy), and total entropies (all quantities are multiplied with temperature), as well as the calculated Gibbs energy (calculated using Phonopy), enthalpy (calculated using Phonopy), and total entropy (multiplied with temperature) for PbSbSeSnSTe high-entropy thermoelectric material are shown to have included the stability of the single-phase high-entropy alloy [8]. It is worth noting that, in general, random alloys have a small fraction of imaginary (negative) phonon frequencies at 0 K, which can be neglected [8]. However, with a significant number of imaginary phonon frequencies, the calculated properties for that crystal structure cannot be considered as it is dynamically unstable due to destabilization of the input structure. A dynamically unstable structure implies that the structure does not satisfy the Born stability criterion, which provides the conditions of mechanical stability of unstressed crystalline structures [85].

The calculation of transport properties is another important attribute to be evaluated for designing and validating high-entropy TE materials. Separate codes can be used to evaluate the individual quantities constituting the evaluation of zT, which can be conveniently interfaced with DFT codes, such as VASP and Wien2K. phonop3py [86] is Python-based open-source software that can calculate phonon–phonon interactions using the supercell

approach to estimate the lattice thermal conductivity as a function of temperature. In addition, the Green–Kubo theory has also been applied to determine the κ_L of high-entropy TE materials with the heat flux data generated using on-the-fly machine-learned force fields [81].

The BoltzTraP (Boltzmann transport properties) [87] code based on Boltzmann transport theory is an open-source program for calculating the semi-classical transport coefficients by smoother Fourier interpolation of band energies based on the space group symmetry of the input structure. This code can be efficiently employed to calculate quantities such as the Seebeck coefficient, electronic thermal conductivity, and electrical conductivity, which can be used to estimate the thermoelectric figure of merit. Figure 12 shows S, σ, κ_e, and PF ($S^2\sigma$) as a function of chemical potential for $Ti_{0.75}HfMo_{0.25}CrGe$ high-entropy TE material calculated using the BoltzTraP code [88]. These essential computational tools for evaluating the figure of merit have made ab initio-based techniques an effective tool for the design of high-performance high-entropy TE materials.

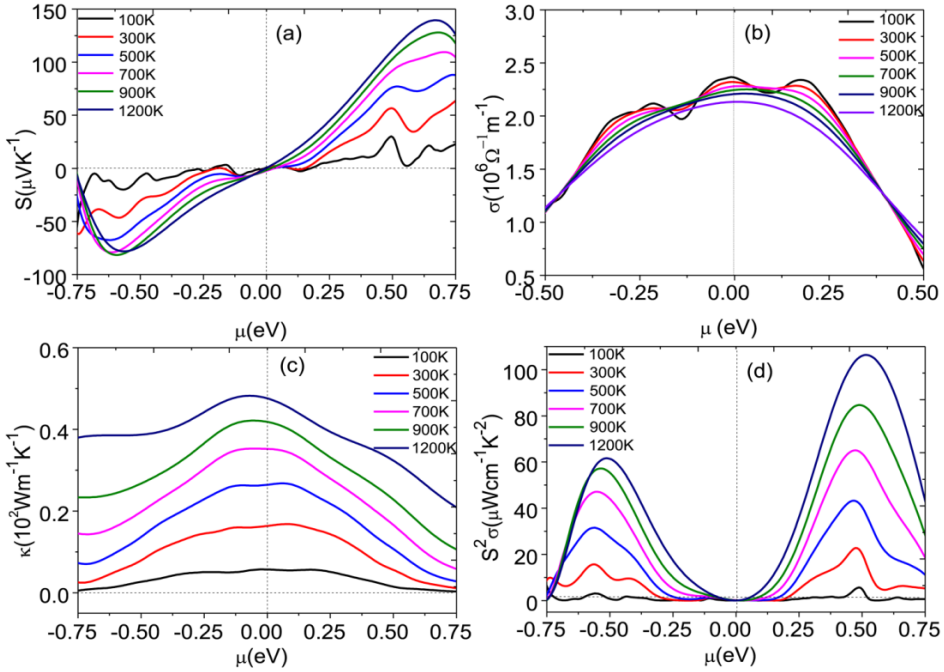

Figure 12. Calculated (**a**) Seebeck coefficient (S), (**b**) electrical conductivity (σ), (**c**) electronic thermal conductivity (κ_e), and (**d**) PF ($S^2\sigma$) for $Ti_{0.75}HfMo_{0.25}CrGe$ high-entropy TE material using BoltzTrap. Reprinted with permission from [88]. Copyright (2018) AIP Publishing.

An extension of the ab initio methods based on DFT is the ab initio molecular dynamics (AIMD) simulation. Classical molecular dynamics simulation generally requires interatomic potentials (or force fields) to describe the interaction between particles, which are not available for many thermoelectric alloy systems. In AIMD calculations, the forces required to describe the interactions are computed on the fly using DFT calculations. This reduces the dependence of AIMD on interatomic potentials to describe the material and circumvents the limited applicability problem due to the lack of interatomic potentials for several alloy systems. Hence, AIMD has become a robust computational tool for modeling complex chemical systems and has been applied to a host of different material systems. However, these calculations are computationally intensive and hence limit their widespread application to large-scale alloy systems. To reduce the computational intensity of these calculations, they are integrated with machine learning techniques that can efficiently determine the required force fields by mapping the atomic configurations to properties with the help of a robust learning algorithm [89]. Machine learning-assisted AIMD simulations have been successfully applied to study the effect of an adaptable sublattice in

stabilizing the single-phase face-centered cubic crystal structure in Mg_2(Si, Ge, Sn, Bi) high-entropy thermoelectric material [38]. The adaptability and flexibility of the loosely bonded Mg sublattice in this structure enables it to release the large lattice strains caused by the high atomic size mismatch among the Si, Ge, Sn, and Bi atoms. This type of distorted lattice was found to efficiently block the transport of phonons and hence lower thermal conductivity for enhancing TE performance. AIMD simulations performed for such a lattice showed that Mg atoms in Mg_2(Si, Ge, Sn, Bi) high-entropy thermoelectric material vibrate in a larger space in comparison to other atoms in the temperature range of 300 to 800 K. Highly diffusive characteristics of the Mg atoms are evident from the plotted trajectories, and the calculated atomic mean square displacement from the AIMD simulations is the highest for Mg at all temperatures (Figure 13a). This implies that the addition of temperature contribution to the ab initio calculations through AIMD simulations deepens the understanding of the structural attributes for stabilizing the single-phase structure in high-entropy thermoelectric materials.

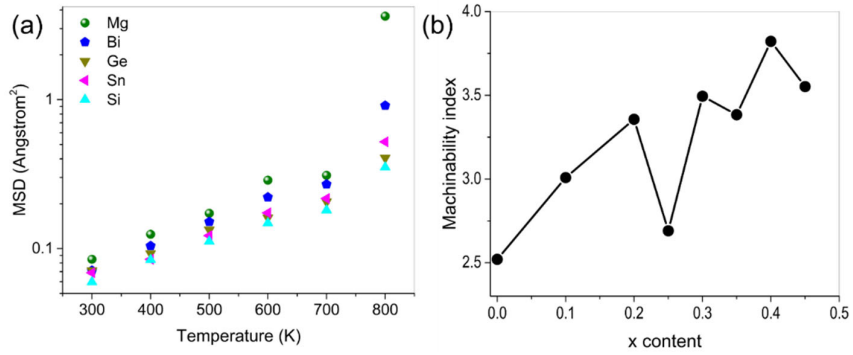

Figure 13. (**a**) Atomic mean square displacement (MSD) for Mg, Si, Ge, Sn, and Bi as a function of temperature obtained using ab initio molecular dynamics simulations for Mg_2(Si, Ge, Ge, Sn, Bi) high-entropy TE material. Reproduced with permission from [38]. Copyright (2023) Royal Society of Chemistry. (**b**) Calculated machinability index for $Pb_{0.99}Sb_{0.012}Se_{1-2x}Te_xS_x$ high-entropy thermoelectric material with varying x content obtained using DFT-based ab initio calculations for a 1080 atom supercell. Reproduced with permission from [90]. Copyright (2023) Springer Nature.

Apart from the TE properties, it is also important to understand the mechanical stability of a designed high-entropy TE material. Ab initio calculations can be employed to deduce the elastic constants in the elastic tensor of the corresponding crystal structure, which can be related to the strength of the material. Hooke's law is used to obtain the elastic constants (C_{ij}), as shown below.

$$\sigma_i = \sum_{j=1}^{6} C_{ij}\epsilon_j \tag{6}$$

where i and j are in the range of 1 to 6. The stress (σ_i) can be obtained by applying different strains (ϵ_j) to the input crystal structure. From these calculated elastic constants, other related quantities, such as the elastic modulus (E), shear modulus (G), bulk modulus (B), and Poisson's ratio (η_P) can be estimated for a material using the Voigt–Reuss–Hill approximation [91,92]. This type of simulation was applied to PbSbSeTeS high-entropy TE material for a 1080-atom supercell, and the elastic constants were calculated for this structure [90]. It should be noted that the machinability of a material is controlled by the elastic constant C_{44} and bulk modulus, which is known as machinability index (μ_M) and is given as follows.

$$\mu_M = \frac{B}{C_{44}} \tag{7}$$

Figure 13b shows the machinability index as a function of alloying content (Se, Te, and S variation) for PbSbSeTeS high-entropy TE material determined by bulk modulus and elastic constants computed using DFT-based ab initio calculations. A higher machinability index indicates that the material has better manufacturability and acts as a measure of the plasticity and lubricating nature of a material [93]. Hence, it is crucial to estimate the machinability index for improving the fabricability of a designed high-entropy thermoelectric material, along with its TE performance evaluation.

5.2. CALPHAD Method

Phase diagrams serve as a roadmap for materials design and process optimization. CALPHAD [94,95] is a powerful technique employed for the generation of phase diagrams for multicomponent alloys of commercial interest. In a nutshell, the CALPHAD technique can be defined as a computer-assisted modeling procedure with experimental and theoretical data as input for generating thermodynamic databases to predict phase equilibria and thermodynamic properties. Although it was initially devised for calculating the phase diagrams in the equilibrium regime, this technique is currently being extended into modeling techniques applied in non-equilibrium regimes (such as diffusion and precipitation simulations). More recently, this technique has also been extended for modeling the thermophysical properties of materials by storing the target property as a function of temperature and chemical composition, which is expected to serve as a useful input for other types of simulations related to thermal and manufacturing process modeling. The major advantage of using this approach is the ease of estimating the properties of multicomponent systems by extrapolation of properties from bounding lower-order systems [95].

For the design of high-entropy thermoelectric alloys, the CALPHAD method can be employed effectively for microstructure design and thermophysical property evaluation. The CALPHAD method provides insights into phase stability and transformation temperatures to achieve compositional uniformity and solubility limits to understand the maximum doping concentration and solidification path for understanding the final microstructure [96]. These attributes directly influence the TE performance of materials with efficient microstructural design. The pseudo-ternary HfNiSn–TiNiSn–ZrNiSn phase diagram from the (Hf, Ti, Zr)NiSn system was plotted using the CALPHAD method to theoretically develop an understanding of the phase separation characteristics, which are useful for enhancing the thermoelectric properties of this alloy system in the temperature range of 500–1300 K [97], as shown in Figure 14a.

Moreover, phase boundary mapping for studying the different thermodynamic states arising due to differing chemical potential within various phase regions of a phase diagram can be applied to understand defect formation energies and related properties [98]. This has been implemented for several stable phases, such as the Zintl phase ($Ca_9Zn_{4+x}Sb_9$) in the Ca-Zn-Sb system [99] and the Yb-doped $CoSb_3$ phase in the Yb-Co-Sb system [100]. In addition, the CALPHAD technique can be conveniently integrated with other approaches, such as phase-field modeling and finite element analysis, to guide microstructural evolution during the fabrication of TE materials [96]. Such modeling efforts are currently not available in the open literature and require further attention to improve the fabricability and microstructural features of TE materials.

Another crucial attribute for assessing the TE behavior of a material using the CALPHAD technique is the determination of the thermophysical properties required for evaluating the figure of merit to tune the TE behavior of a material. Thermophysical property databases are currently available for computing properties such as thermal conductivity and electrical resistivity. Although these properties can be evaluated using ab initio methods, as explained in the previous subsection, the CALPHAD approach outshines the ab initio calculations in predicting properties as a function of composition and temperature coupled with phase equilibria of the material. Hence, the values calculated using ab initio calculations can serve as useful inputs for the development of CALPHAD-based thermophysical property databases. In addition, other useful properties, such as carrier

concentration [101] and scattering strength [102], can be evaluated using this method, which will complement the multicomponent thermoelectric material design.

Currently, CALPHAD-type assessments are available for carrier concentration in binary Pb-Se systems [101], which will be useful for extension to the multicomponent high-entropy alloy-type systems (Figure 14b). However, additional efforts are necessary to implement this approach in other well-known thermoelectric material systems. Moreover, the scattering strength (Γ), which quantifies the reduction of the electronic and thermal transport in alloy mixtures, had a functional form similar to the excess Gibbs energy (known as the Redlich Kister polynomial) in the CALPHAD method, which can be extrapolated to multicomponent systems, as shown in Figure 14c [102]. This proves that CALPHAD-type expressions can be developed for several thermophysical properties that are required to determine the TE behavior of lower-order subsystems (binary and ternary systems), and the extrapolation scheme implemented using the CALPHAD method can predict the properties of a multicomponent system with fair accuracy, aiding the design of new high-entropy TE materials.

At present, there is a dearth of thermodynamic and thermophysical databases for well-known thermoelectric binary and ternary alloy systems. This limits the possibility of exploring the effectiveness of the CALPHAD method for the design of high-entropy TE materials as an extension of the currently known TE materials. Reliable modeling efforts are crucial to building these databases with high fidelity for lower-order (binary and ternary) systems. This necessitates thorough experimental investigations and precise ab initio calculations to design these multicomponent alloys. Efficient extrapolation to high-order systems is possible only if the databases for lower-order systems are of high fidelity. The thermodynamic and thermophysical databases can be efficiently used for high-throughput alloy screening with composition, phase equilibria, and target property as the attributes for efficient discovery of new high-entropy TE materials in an expanded chemical space.

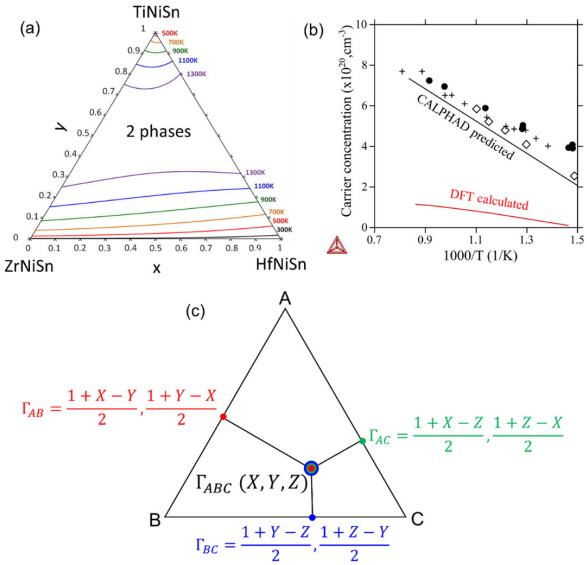

Figure 14. (**a**) Isotherms at different temperatures in the pseudo-ternary HfNiSn-TiNiSn-ZrNiSn system with the phase limit of Ti-rich and Hf,Zr-rich phases indicated to determine the 2-phase region. Reprinted with permission from [97]. Copyright (2017) Elsevier. (**b**) Comparison between the carrier concentration of PbSe phase under Pb-rich conditions in the Pb-Se system determined using CALPHAD- and DFT-based ab initio calculations along with experimental data. Reproduced with permission from [101]. Copyright (2019) Elsevier. (**c**) Schematic showing the geometric extrapolation by the Muggianu model for determining the ternary excess quantity from a weighted sum of corresponding binary excess quantities. Reproduced with permission from [102]. Copyright (2022) Wiley-VCH.

5.3. Data-Driven Methods

With the advent of artificial intelligence, the recent trend for new material discovery is to apply machine learning and data-driven screening approaches in the multielement chemical space. Materials informatics is a research field that applies the principles of informatics to the materials science and engineering fields [103]. It is attracting considerable attention due to its ability to predict material properties and accelerate the development of new materials. It not only significantly lessens the development cycle for new materials but also offers a novel and efficient approach to advancing materials science and engineering. A huge volume of datasets will be required for screening the optimum composition and properties with good accuracy to efficiently implement the machine learning and data-driven techniques. Although there are few works reporting the application of materials informatics for thermoelectric compounds [104–107], efforts toward the design of high-entropy thermoelectric materials using data-driven methods are very scarce. The cation–sulfur bond length of diamond-like compounds containing Cu and S identified by screening the Inorganic Crystal Structure Database (ICSD) was used as a chemical descriptor to design a high-entropy sulfide with good thermoelectric performance, as shown in Figure 15a [107]. The developed data-driven model chose suitable elements to reduce the enthalpy of formation and, hence, increase the probability of forming a single-phase solid solution. Using this approach, two high-entropy sulfides with high zT, namely, $Cu_5SnMgGeZnS_9$, which was metallic in nature, and $Cu_3SnMgInZnS_7$, with semiconducting properties, finally claim that this approach can be implemented to discover new high-entropy functional materials in a largely unexplored multielement chemical space. Similarly, optimal composition ranges with high thermoelectric performance were discovered for Cu_2S–Cu_2Se–Cu_2Te multicomponent solid solutions using a data-driven searching approach by predicting the contouring diagrams from known experimental data for different attributes, such as Hall carrier concentration, weighted mobility, electrical conductivity, Seebeck coefficient, thermal conductivity, and figure of merit (Figure 15b) [108]. Although machine learning has succeeded in predicting unobserved data by learning complex patterns, the ability to interpret what a model has learned is receiving great attention. Therefore, an interpretable machine learning method was formulated such that the relevant knowledge from a machine learning model concerning relationships either contained within the data or learned from the model could be extracted [109]. An interpretable machine learning framework was recently employed to design a GeTe-based high-entropy TE material under different temperatures and chemical compositions [110]. The initial set of material descriptors chosen were atomic number, atomic mass, atomic radius, molar volume, electronegativity, ionization energy, valence electrons, and temperature. Eventually, with the aid of the Shapley additive explanations (SHAP) method [111], the descriptor found to have the greatest effect on the figure of merit of thermoelectric materials was temperature, which was followed by molar volume and electronegativity (Figure 16). Using this framework, GeTeSbSnSe high-entropy TE material with improved TE performance and low-cost requirement was designed. With only a few works available in the literature, it is evident that further efforts directed toward the use of data-driven methods for the discovery of high-entropy TE materials are necessary for accelerated design of new alloys.

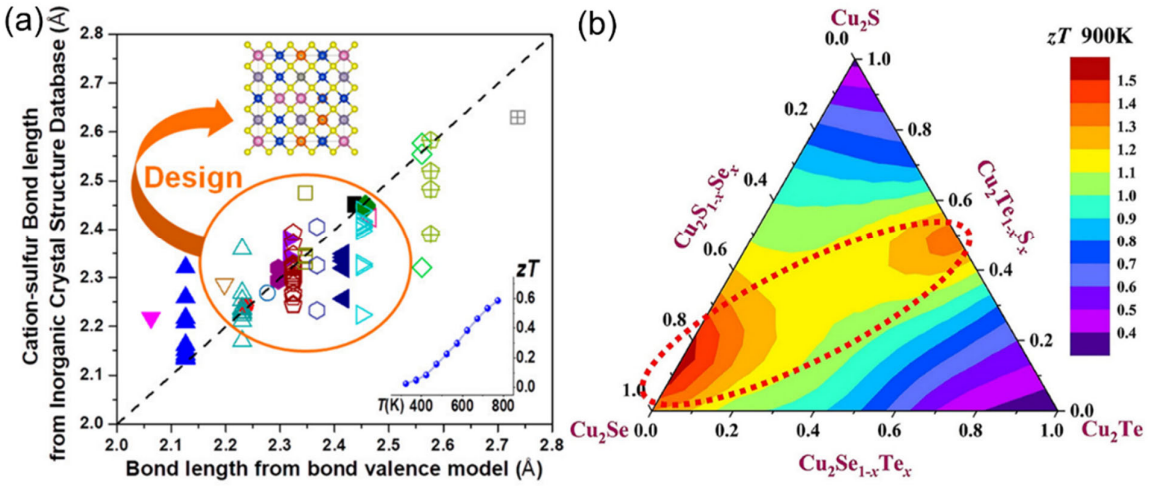

Figure 15. (**a**) Data-driven design of diamond-like compounds containing Cu and S with high TE performance (inset) using the cation–sulfur bond length as a chemical descriptor. Reprinted with permission from [107]. Copyright (2018) American Society of Chemistry. (**b**) Contour diagram of zT for Cu_2S–Cu_2Se–Cu_2Te solid solutions showing that the optimum compositions with high TE performance are near Cu_2Se and in the middle of Cu_2S and Cu_2Te (dashed circle). Reprinted with permission from [108]. Copyright (2022) Elsevier.

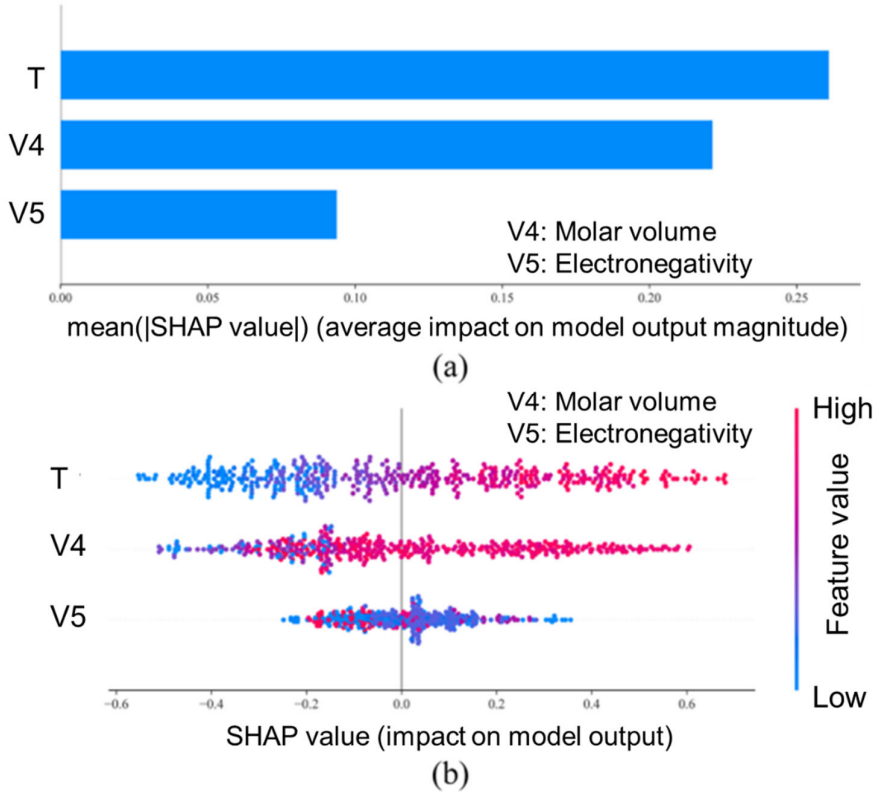

Figure 16. (**a**) Average impact on model output magnitude (y-axis denotes the features, and x-axis denotes the average of the absolute values of the SHAP values for all samples influenced by each feature). (**b**) Effect of each feature on the output of the model (y-axis denotes the features, and x-axis denotes the SHAP values of all samples influenced by each feature). Reprinted with permission from [110]. Copyright (2023) American Society of Chemistry.

6. Concluding Remarks

Entropy engineering in TE materials represents a cutting-edge area of research with significant potential for revolutionizing energy conversion technologies. The reviewed

advancements underscore the importance of a multidisciplinary approach to optimizing entropy-related properties and pave the way for the next generation of efficient TE devices.

The challenges lie in how to design elements that can enhance m^* and S and minimize κ_L simultaneously, with adequate carrier concentration to compensate for the deterioration of μ_H due to an increase in ΔS_{conf}. Moreover, what to alloy, how much to alloy, and which site(s) to alloy/dope should be the design strategy while adopting entropy engineering for TE materials. The effects of entropy engineering can be summarized as follows:

(1) ΔS_{conf} increases with an increase in the number of elements. By increasing ΔS_{conf}, the solid solubility is extended, and more stable and high-symmetry crystal structures are formed [30,112].

(2) ΔS_{conf} reduces the phase transition temperature, thereby extending the stability region of high-symmetry crystal structures over a wide range of temperatures [50]. The high-symmetry crystal structures lead to large band degeneracy and form overlapping or multiple bands near the Fermi level. This results in more equivalent positions in real and reciprocal space, thereby increasing the density of states and m^*, which in turn improves S [30,50,113].

The usage of multiple elements with different atomic sizes and masses results in significant fluctuations of strain fields associated with them, causing severe lattice distortion. This further reduces phonon velocity, increases scattering, and reduces κ_L. However, the lattice distortion can also affect μ_H and σ, which may deteriorate zT performance. Therefore, a comprehensive consideration to compensate for the reduction of μ_H by improving S and reducing κ_L is needed to obtain a high zT [102,113]. It is worth noting that it is crucial to further employ electron microscopy, atomic force microscopy, and atomic probe tomography and develop new characterization methods to analyze and understand the electron/phonon transport and mechanical behaviors on microstructure and defect levels since many fundamental mechanisms based on entropy-engineering are still unclear. The mechanical behavior of TE devices and materials depends largely on the microstructure, composition, phase purity, grain size, and phase stability at high temperatures. Recently, the incorporation of architected structures has been utilized to improve the toughening mechanisms of TE alloys [58,114,115]. However, more studies are required to draw constructive conclusions about high-entropy TE materials. It is hypothesized that lattice distortion and solid solution strengthening due to the use of multicomponent elements in TE alloys results in their higher performance. The area is still developing, and there is a significant scope for in-depth research.

While entropy engineering has shown remarkable progress, challenges remain. Achieving a delicate balance between enhanced entropy and other material properties is essential. Moreover, scalable synthesis methods for these advanced materials need to be developed for practical applications. Collaborative efforts across disciplines, including materials science, physics, and engineering, will be crucial to overcoming these challenges. As research in this field continues to evolve, the prospects for sustainable and energy-efficient solutions appear increasingly promising.

Author Contributions: Conceptualization, S.G. and W.L.; methodology, S.G., L.R., S.S. and W.L.; validation, S.G., L.R., S.S. and W.L.; data curation, S.G., L.R., S.S. and W.L.; writing—original draft preparation, S.G., L.R. and S.S.; writing—review and editing, S.G., L.R., S.S. and W.L.; supervision, W.L.; project administration, W.L. All authors have read and agreed to the published version of the manuscript.

Funding: S.G. and W.L. acknowledge the financial support from the Army RIF program (contract number W911W6-19-C-0083).

Data Availability Statement: Not applicable.

Conflicts of Interest: The authors declare no conflict of interest.

References

1. Kanatzidis, M.G.; Chang, C. High-Entropy Thermoelectric Materials Emerging. *Mater. Lab* **2023**, *2*, 220048. [CrossRef]
2. Dong, J.; Yan, Q.; Gao, J. High Entropy Strategy on Thermoelectric Materials. *Mater. Lab* **2023**, *2*, 230001. [CrossRef]
3. Yeh, J.W.; Chen, S.K.; Lin, S.J.; Gan, J.Y.; Chin, T.S.; Shun, T.T.; Tsau, C.H.; Chang, S.Y. Nanostructured High-Entropy Alloys with Multiple Principal Elements: Novel Alloy Design Concepts and Outcomes. *Adv. Eng. Mater.* **2004**, *6*, 299. [CrossRef]
4. Cantor, B.; Chang, I.T.H.; Knight, P.; Vincent, A.J.B. Microstructural Development in Equiatomic Multicomponent Alloys. *Mater. Sci. Eng. A* **2004**, *213*, 375–377. [CrossRef]
5. Murty, B.S.; Yeh, J.-W.; Ranganathan, S.; Bhattacharjee, P.P. *High-Entropy Alloys*, 2nd ed.; Elsevier: Amsterdam, The Netherlands, 2019.
6. Xin, Y.; Li, S.; Qian, Y.; Zhu, W.; Yuan, H.; Jiang, P.; Guo, R.; Wang, L. High-Entropy Alloys as a Platform for Catalysis: Progress, Challenges, and Opportunities. *ACS Catal.* **2020**, *10*, 11280. [CrossRef]
7. Fan, L.; Li, Y.; Li, J.; Xiang, Q.; Wang, X.; Wen, T.; Zhong, Z.; Liao, Y. High entropy dielectrics. *J. Adv. Dielectr.* **2023**, *13*, 2350014. [CrossRef]
8. Jiang, B.; Yu, Y.; Cui, J.; Liu, X.; Xie, L.; Liao, J.; Zhang, Q.; Huang, Y.; Ning, S.; Jia, B.; et al. High-Entropy-Stabilized Chalcogenides with High Thermoelectric Performance. *Science* **2021**, *371*, 830. [CrossRef] [PubMed]
9. Jiang, B.; Yu, Y.; Chen, H.; Cui, J.; Liu, X.; Xie, L.; He, J. Entropy Engineering Promotes Thermoelectric Performance in P-Type Chalcogenides. *Nat. Commun.* **2021**, *12*, 3234. [CrossRef]
10. Jiang, B.; Wang, W.; Liu, S.; Wang, Y.; Wang, C.; Chen, Y.; Xie, L.; Huang, M.; He, J. High Figure-of-Merit and Power Generation in High-Entropy GeTe-Based Thermoelectrics. *Science* **2022**, *377*, 208. [CrossRef]
11. Chen, K.; Zhang, R.; Bos, J.W.G.; Reece, M.J. Synthesis and Thermoelectric Properties of High-Entropy Half-Heusler MFe1−xCoxSb (M = Equimolar Ti, Zr, Hf, V, Nb, Ta). *J. Alloys Compd.* **2022**, *892*, 162045. [CrossRef]
12. Yan, J.; Liu, F.; Ma, G.; Gong, B.; Zhu, J.; Wang, X.; Ao, W.; Zhang, C.; Li, Y.; Li, J. Suppression of the Lattice Thermal Conductivity in NbFeSb-Based Half-Heusler Thermoelectric Materials through High Entropy Effects. *Scr. Mater.* **2018**, *157*, 129. [CrossRef]
13. Li, W.; Goyal, G.K.; Stokes, D.; Raman, L.; Ghosh, S.; Sharma, S.; Nozariasbmarz, A.; Liu, N.; Singh, S.; Zhang, Y.; et al. High-Performance Skutterudite/Half-Heusler Cascaded Thermoelectric Module Using the Transient Liquid Phase Sintering Joining Technique. *ACS Appl. Mater. Interfaces* **2023**, *15*, 2961. [CrossRef] [PubMed]
14. Li, W.; Wang, J.; Poudel, B.; Kang, H.B.; Huxtable, S.; Nozariasbmarz, A.; Saparamadu, U.; Priya, S. Filiform Metal Silver Nanoinclusions To Enhance Thermoelectric Performance of P-Type Ca 3 Co 4 O 9+δ Oxide. *ACS Appl. Mater. Interfaces* **2019**, *11*, 42131. [CrossRef] [PubMed]
15. Li, W.; Stokes, D.; Poudel, B.; Saparamadu, U.; Nozariasbmarz, A.; Kang, H.B.; Priya, S. High-Efficiency Skutterudite Modules at a Low Temperature Gradient. *Energies* **2019**, *12*, 4292. [CrossRef]
16. Nie, G.; Li, W.; Guo, J.; Yamamoto, A.; Kimura, K.; Zhang, X.; Isaacs, E.B.; Dravid, V.; Wolverton, C.; Kanatzidis, M.G.; et al. High Performance Thermoelectric Module through Isotype Bulk Heterojunction Engineering of Skutterudite Materials. *Nano Energy* **2019**, *66*, 104193. [CrossRef]
17. Li, W.; Ghosh, S.; Liu, N.; Poudel, B. Half-Heusler Thermoelectrics: Advances from Materials Fundamental to Device Engineering. *Joule* **2024**, *in press*. [CrossRef]
18. Zhang, Q.; Guo, Z.; Wang, R.; Tan, X.; Song, K.; Sun, P.; Hu, H.; Cui, C.; Liu, G.Q.; Jiang, J. High-Performance Thermoelectric Material and Module Driven by Medium-Entropy Engineering in SnTe. *Adv. Funct. Mater.* **2022**, *32*, 2205458. [CrossRef]
19. Zhu, H.; Li, W.; Nozariasbmarz, A.; Liu, N.; Zhang, Y.; Priya, S.; Poudel, B. Half-Heusler Alloys as Emerging High Power Density Thermoelectric Cooling Materials. *Nat. Commun.* **2023**, *14*, 3300. [CrossRef] [PubMed]
20. Li, W.; Poudel, B.; Nozariasbmarz, A.; Sriramdas, R.; Zhu, H.; Kang, H.B.; Priya, S. Bismuth Telluride/Half-Heusler Segmented Thermoelectric Unicouple Modules Provide 12% Conversion Efficiency. *Adv. Energy Mater.* **2020**, *10*, 2001924. [CrossRef]
21. Nozariasbmarz, A.; Saparamadu, U.; Li, W.; Kang, H.B.; Dettor, C.; Zhu, H.; Poudel, B.; Priya, S. High-Performance Half-Heusler Thermoelectric Devices through Direct Bonding Technique. *J. Power Sources* **2021**, *493*, 229695. [CrossRef]
22. Snyder, G.J.; Toberer, E.S. Complex Thermoelectric Materials. *Nat. Mater.* **2008**, *7*, 105. [CrossRef] [PubMed]
23. Zhang, Y.; Li, Z.; Singh, S.; Nozariasbmarz, A.; Li, W.; Genç, A.; Xia, Y.; Zheng, L.; Lee, S.H.; Karan, S.K.; et al. Defect-Engineering-Stabilized AgSbTe 2 with High Thermoelectric Performance. *Adv. Mater.* **2023**, *35*, 2208994. [CrossRef] [PubMed]
24. Zhu, H.; He, R.; Mao, J.; Zhu, Q.; Li, C.; Sun, J.; Ren, W.; Wang, Y.; Liu, Z.; Tang, Z.; et al. Discovery of ZrCoBi Based Half Heuslers with High Thermoelectric Conversion Efficiency. *Nat. Commun.* **2018**, *9*, 2497. [CrossRef] [PubMed]
25. Li, W.; Wang, J.; Xie, Y.; Gray, J.L.; Heremans, J.J.; Kang, H.B.; Poudel, B.; Huxtable, S.T.; Priya, S. Enhanced Thermoelectric Performance of Yb-Single-Filled Skutterudite by Ultralow Thermal Conductivity. *Chem. Mater.* **2019**, *31*, 862. [CrossRef]
26. Li, W.; Poudel, B.; Kishore, R.A.; Nozariasbmarz, A.; Liu, N.; Zhang, Y.; Priya, S. Toward High Conversion Efficiency of Thermoelectric Modules through Synergistical Optimization of Layered Materials. *Adv. Mater.* **2023**, *35*, 2210407. [CrossRef] [PubMed]
27. Kang, H.B.; Poudel, B.; Li, W.; Lee, H.; Saparamadu, U.; Nozariasbmarz, A.; Kang, M.G.; Gupta, A.; Heremans, J.J.; Priya, S. Decoupled Phononic-Electronic Transport in Multi-Phase n-Type Half-Heusler Nanocomposites Enabling Efficient High Temperature Power Generation. *Mater. Today* **2020**, *36*, 63. [CrossRef]
28. Wang, H.; He, Q.; Gao, X.; Shang, Y.; Zhu, W.; Zhao, W.; Chen, Z.; Gong, H.; Yang, Y. Multifunctional High Entropy Alloys Enabled by Severe Lattice Distortion. *Adv. Mater.* **2023**, *36*, e2305453. [CrossRef] [PubMed]

29. Schweidler, S.; Botros, M.; Strauss, F.; Wang, Q.; Ma, Y.; Velasco, L.; Marques, G.C.; Sarkar, A.; Kübel, C.; Hahn, H.; et al. High-Entropy Materials for Energy and Electronic Applications. *Nat. Rev. Mater.* **2024**, *9*, 266–281. [CrossRef]
30. Toda-Caraballo, I.; Rivera-Díaz-del-Castillo, P.E.J. A Criterion for the Formation of High Entropy Alloys Based on Lattice Distortion. *Intermetallics* **2016**, *71*, 76. [CrossRef]
31. Usharani, N.J.; Shringi, R.; Sanghavi, H.; Subramanian, S.; Bhattacharya, S.S.; Size, R.O. Alio-/Multi-Valency and Non-Stoichiometry in the Synthesis of Phase-Pure High Entropy Oxide (Co,Cu,Mg,Na,Ni,Zn)O. *Dalton Trans.* **2020**, *49*, 7123. [CrossRef]
32. Fultz, B. Vibrational Thermodynamics of Materials. *Prog. Mater. Sci.* **2010**, *55*, 247. [CrossRef]
33. Xia, J.; Yang, J.; Wang, Y.; Jia, B.; Li, S.; Sun, K.; Zhao, Q.; Mao, D.; Li, H.F.; He, J. Synergistic Entropy Engineering with Vacancies: Unraveling the Cocktail Effect for Extraordinary Thermoelectric Performance in SnTe-Based Materials. *Adv. Funct. Mater.* **2024**, *2024*, 2401635. [CrossRef]
34. Liu, R.; Chen, H.; Zhao, K.; Qin, Y.; Jiang, B.; Zhang, T.; Sha, G.; Shi, X.; Uher, C.; Zhang, W.; et al. Entropy as a Gene-Like Performance Indicator Promoting Thermoelectric Materials. *Adv. Mater.* **2017**, *29*, 1702712. [CrossRef] [PubMed]
35. Ren, W.; Song, Q.; Zhu, H.; Mao, J.; You, L.; Gamage, G.; Zhou, J.; Zhou, T.; Jiang, J.; Wang, C.; et al. Intermediate-Level Doping Strategy to Simultaneously Optimize Power Factor and Phonon Thermal Conductivity for Improving Thermoelectric Figure of Merit. *Mater. Today Phys.* **2020**, *15*, 100250. [CrossRef]
36. Qiu, Y.; Jin, Y.; Wang, D.; He, W.; Zhao, L.D.; Guan, M.; Peng, S.; Liu, R.; Gao, X. Realizing High Thermoelectric Performance in GeTe through Decreasing the Phase Transition Temperature via Entropy Engineering. *J. Mater. Chem. A Mater.* **2019**, *7*, 26393. [CrossRef]
37. Ma, Z.; Luo, Y.; Li, W.; Xu, T.; Wei, Y.; Li, C.; Haruna, A.Y.; Jiang, Q.; Zhang, D.; Yang, J. High Thermoelectric Performance and Low Lattice Thermal Conductivity in Lattice-Distorted High-Entropy Semiconductors AgMnSn1-XPbxSbTe4. *Chem. Mater.* **2022**, *34*, 8959. [CrossRef]
38. Gao, H.; Zhao, K.; Wuliji, H.; Zhu, M.; Xu, B.; Lin, H.; Fei, L.; Zhang, H.; Zhou, Z.; Lei, J.; et al. Adaptable Sublattice Stabilized High-Entropy Materials with Superior Thermoelectric Performance. *Energy Environ. Sci.* **2023**, *16*, 6046. [CrossRef]
39. Fan, Z.; Wang, H.; Wu, Y.; Liu, X.J.; Lu, Z.P. Thermoelectric High-Entropy Alloys with Low Lattice Thermal Conductivity. *RSC Adv.* **2016**, *6*, 52164. [CrossRef]
40. Fan, Z.; Wang, H.; Wu, Y.; Liu, X.; Lu, Z. Thermoelectric Performance of PbSnTeSe High-Entropy Alloys. *Mater. Res. Lett.* **2017**, *5*, 187. [CrossRef]
41. Hu, L.; Zhang, Y.; Wu, H.; Li, J.; Li, Y.; Mckenna, M.; He, J.; Liu, F.; Pennycook, S.J.; Zeng, X. Entropy Engineering of SnTe: Multi-Principal-Element Alloying Leading to Ultralow Lattice Thermal Conductivity and State-of-the-Art Thermoelectric Performance. *Adv. Energy Mater.* **2018**, *8*, 1802116. [CrossRef]
42. Jiang, B.; Qiu, P.; Chen, H.; Huang, J.; Mao, T.; Wang, Y.; Song, Q.; Ren, D.; Shi, X.; Chen, L. Entropy Optimized Phase Transitions and Improved Thermoelectric Performance in N-Type Liquid-like Ag9GaSe6 Materials. *Mater. Today Phys.* **2018**, *5*, 20. [CrossRef]
43. Karati, A.; Nagini, M.; Ghosh, S.; Shabadi, R.; Pradeep, K.G.; Mallik, R.C.; Murty, B.S.; Varadaraju, U.V. Ti $_2$NiCoSnSb—A New Half-Heusler Type High-Entropy Alloy Showing Simultaneous Increase in Seebeck Coefficient and Electrical Conductivity for Thermoelectric Applications. *Sci. Rep.* **2019**, *9*, 5331. [CrossRef] [PubMed]
44. Luo, Y.; Hao, S.; Cai, S.; Slade, T.J.; Luo, Z.Z.; Dravid, V.P.; Wolverton, C.; Yan, Q.; Kanatzidis, M.G. High Thermoelectric Performance in the New Cubic Semiconductor AgSnSbSe3by High-Entropy Engineering. *J. Am. Chem. Soc.* **2020**, *142*, 15187. [CrossRef]
45. Yamashita, A.; Goto, Y.; Miura, A.; Moriyoshi, C.; Kuroiwa, Y.; Mizuguchi, Y. N-Type Thermoelectric Metal Chalcogenide (Ag,Pb,Bi)(S,Se,Te) Designed by Multi-Site-Type High-Entropy Alloying. *Mater. Res. Lett.* **2021**, *9*, 366. [CrossRef]
46. Wang, X.; Yao, H.; Zhang, Z.; Li, X.; Chen, C.; Yin, L.; Hu, K.; Yan, Y.; Li, Z.; Yu, B.; et al. Enhanced Thermoelectric Performance in High Entropy Alloys Sn 0.25 Pb 0.25 Mn 0.25 Ge 0.25 Te. *ACS Appl. Mater. Interfaces* **2021**, *13*, 18638. [CrossRef] [PubMed]
47. Ma, Z.; Xu, T.; Li, W.; Cheng, Y.; Li, J.; Zhang, D.; Jiang, Q.; Luo, Y.; Yang, J. High Entropy Semiconductor AgMnGeSbTe4 with Desirable Thermoelectric Performance. *Adv. Funct. Mater.* **2021**, *31*, 2103197. [CrossRef]
48. Cai, J.; Yang, J.; Liu, G.; Wang, H.; Shi, F.; Tan, X.; Ge, Z.; Jiang, J. Ultralow Thermal Conductivity and Improved ZT of CuInTe2 by High-Entropy Structure Design. *Mater. Today Phys.* **2021**, *18*, 100394. [CrossRef]
49. Zhang, W.; Lou, Y.; Dong, H.; Wu, F.; Tiwari, J.; Shi, Z.; Feng, T.; Pantelides, S.T.; Xu, B. Phase-Engineered High-Entropy Metastable FCC Cu2−yAgy(InxSn1−x)Se2S Nanomaterials with High Thermoelectric Performance. *Chem. Sci.* **2022**, *13*, 10461. [CrossRef] [PubMed]
50. Huang, Y.; Zhi, S.; Zhang, S.; Yao, W.; Ao, W.; Zhang, C.; Liu, F.; Li, J.; Hu, L. Regulating the Configurational Entropy to Improve the Thermoelectric Properties of (GeTe)1−x(MnZnCdTe3)x Alloys. *Materials* **2022**, *15*, 6798. [CrossRef]
51. Zhang, M.; Cai, J.; Gao, F.; Zhang, Z.; Li, M.; Chen, Z.; Wang, Y.; Hu, D.; Tan, X.; Liu, G.; et al. Improved Thermoelectric Performance of P-Type PbTe by Entropy Engineering and Temperature-Dependent Precipitates. *ACS Appl. Mater. Interfaces* **2024**, *16*, 907. [CrossRef]
52. Yang, J.; Meisner, G.P.; Chen, L. Strain Field Fluctuation Effects on Lattice Thermal Conductivity of ZrNiSn-Based Thermoelectric Compounds. *Appl. Phys. Lett.* **2004**, *85*, 1140. [CrossRef]
53. Chen, R.; Yan, Y.; Zhang, W.; Liu, F.; Kang, H.; Guo, E.; Chen, Z.; Wang, T. Enhanced Thermoelectric Properties of Zr0.85–x Hf x Nb0.15–y Ta y CoSb Medium-Entropy Alloys: Tradeoff between "What to Alloy" and "How Much to Alloy. *Chem. Mater.* **2023**, *35*, 2202–2212. [CrossRef]

54. Zhang, X.; Huang, M.; Li, H.; Chen, J.; Xu, P.; Xu, B.; Wang, Y.; Tang, G.; Yang, S. Ultralow Lattice Thermal Conductivity and Improved Thermoelectric Performance in a Hf-Free Half-Heusler Compound Modulated by Entropy Engineering. *J. Mater. Chem. A Mater.* **2023**, *11*, 8150–8161. [CrossRef]
55. Banerjee, R.; Chatterjee, S.; Ranjan, M.; Bhattacharya, T.; Mukherjee, S.; Jana, S.S.; Dwivedi, A.; Maiti, T. High-Entropy Perovskites: An Emergent Class of Oxide Thermoelectrics with Ultralow Thermal Conductivity. *ACS Sustain. Chem. Eng.* **2020**, *8*, 17022. [CrossRef]
56. Zheng, Y.; Zou, M.; Zhang, W.; Yi, D.; Lan, J.; Nan, C.-W.; Lin, Y.-H. Electrical and Thermal Transport Behaviours of High-Entropy Perovskite Thermoelectric Oxides. *J. Adv. Ceram.* **2021**, *10*, 377. [CrossRef]
57. Bao, X.; Hou, S.; Wu, Z.; Wang, X.; Yin, L.; Liu, Y.; He, H.; Duan, S.; Wang, B.; Mao, J.; et al. Mechanical Properties of Thermoelectric Generators. *J. Mater. Sci. Technol.* **2023**, *148*, 64. [CrossRef]
58. Wu, L.; Feng, X.; Cao, K.; Li, G. Toughening Thermoelectric Materials: From Mechanisms to Applications. *Int. J. Mol. Sci.* **2023**, *24*, 6325. [CrossRef]
59. He, R.; Gahlawat, S.; Guo, C.; Chen, S.; Dahal, T.; Zhang, H.; Liu, W.; Zhang, Q.; Chere, E.; White, K.; et al. Studies on Mechanical Properties of Thermoelectric Materials by Nanoindentation. *Phys. Status Solidi A Appl. Mater. Sci.* **2015**, *212*, 2191. [CrossRef]
60. Tavares, S.; Yang, K.; Meyers, M.A. Heusler Alloys: Past, Properties, New Alloys, and Prospects. *Prog. Mater. Sci.* **2023**, *132*, 101017. [CrossRef]
61. Rogl, G.; Rogl, P. Mechanical Properties of Skutterudites. *Sci. Adv. Mater.* **2011**, *3*, 517. [CrossRef]
62. Lu, T.; Wang, B.; Li, G.; Yang, J.; Zhang, X.; Chen, N.; Liu, T.-H.; Yang, R.; Niu, P.; Kan, Z.; et al. Synergistically Enhanced Thermoelectric and Mechanical Performance of Bi2Te3 via Industrial Scalable Hot Extrusion Method for Cooling and Power Generation Applications. *Mater. Today Phys.* **2023**, *32*, 101035. [CrossRef]
63. Guttmann, G.M.; Gelbstein, Y. *Mechanical Properties of Thermoelectric Materials for Practical Applications, in Bringing Thermoelectricity into Reality*; InTech: Rijeka, Croatia, 2018.
64. Verges, M.A.; Schilling, P.J.; Germond, J.D.; Upadhyay, P.; Miller, W.K.; Takas, N.J.; Poudeu, P.F.P. Indentation Testing of Bulk $Zr_{0.5}Hf_{0.5}Co_{1-x}Ir_xSb_{0.99}Sn_{0.01}$ Half-Heusler Alloys. *MRS Proc.* **2010**, *1267*, 1267. [CrossRef]
65. O'Connor, C.J. *Nanostructured Composite Materials for High Temperature Thermoelectric Energy Conversion*; New Orleans University: New Orleans, LA, USA, 2012; p. 0026.
66. Fan, X. *Mechanical Characterization of Hydroxyapatite, Thermoelectric Materials and Doped Ceria*; Michigan State University: East Lansing, MI, USA, 2013.
67. Rogl, G.; Grytsiv, A.; Gürth, M.; Tavassoli, A.; Ebner, C.; Wünschek, A.; Puchegger, S.; Soprunyuk, V.; Schranz, W.; Bauer, E.; et al. Mechanical Properties of Half-Heusler Alloys. *Acta Mater.* **2016**, *107*, 178. [CrossRef]
68. Jung, D.Y.; Kurosaki, K.; Kim, C.E.; Muta, H.; Yamanaka, S. Thermal Expansion and Melting Temperature of the Half-Heusler Compounds: MNiSn (M = Ti, Zr, Hf). *J. Alloys Compd.* **2010**, *489*, 328. [CrossRef]
69. Lu, Y.; Zhang, P.; Wang, J.; Song, Q.; Chen, Z.; Wang, Y.; Chen, L.; Bai, S.; Wang, W. Temperature-Dependent Compression Properties and Failure Mechanisms of ZrNiSn-Based Half-Heusler Thermoelectric Compounds. *J. Mater. Sci. Technol.* **2024**, *193*, 29–36. [CrossRef]
70. Al Malki, M.M.; Qiu, Q.; Zhu, T.; Snyder, G.J.; Dunand, D.C. Creep Behavior and Postcreep Thermoelectric Performance of the N-Type Half-Heusler Alloy Hf0.3Zr0.7NiSn0.98Sb0.02. *Mater. Today Phys.* **2019**, *9*, 100134. [CrossRef]
71. Zhang, L.; Shi, X.L.; Yang, Y.L.; Chen, Z.G. Flexible Thermoelectric Materials and Devices: From Materials to Applications. *Mater. Today* **2021**, *46*, 62–108. [CrossRef]
72. Aljaghtham, M. A Comparative Performance Analysis of Thermoelectric Generators with a Novel Leg Geometries. *Energy Rep.* **2024**, *11*, 859. [CrossRef]
73. Li, M.; Dizaji, H.S.; Asaadi, S.; Jarad, F.; Anqi, A.E.; Wae-hayee, M. Thermo-Economic, Exergetic and Mechanical Analysis of Thermoelectric Generator with Hollow Leg Structure; Impact of Leg Cross-Section Shape and Hollow-to-Filled Area Ratio. *Case Stud. Therm. Eng.* **2021**, *27*, 101314. [CrossRef]
74. Kreese, G.; Furthmuller, J. Efficiency of Ab-Initio Total Energy Calculations for Metals and Semiconductors Using a Plane-Wave Basis Set. *Comput. Mater. Sci.* **1996**, *6*, 15. [CrossRef]
75. Kreese, G.; Furthmuller, J. Efficient Iterative Schemes for Ab Initio Total-Energy Calculations Using a Plane-Wave Basis Set. *Phys. Rev. B* **1996**, *54*, 11169. [CrossRef] [PubMed]
76. Blaha, P.; Schwarz, K.; Tran, F.; Laskowski, R.; Madsen, G.K.H.; Marks, L.D. WIEN2k: An APW+lo Program for Calculating the Properties of Solids. *J. Chem. Phys.* **2020**, *152*, 074101. [CrossRef] [PubMed]
77. Van De Walle, A.; Tiwary, P.; De Jong, M.; Olmsted, D.L.; Asta, M.; Dick, A.; Shin, D.; Wang, Y.; Chen, L.Q.; Liu, Z.K. Efficient Stochastic Generation of Special Quasirandom Structures. *Calphad* **2013**, *42*, 13. [CrossRef]
78. Van De Walle, A.; Asta, M.; Cederb, G. The Alloy Theoretic Automated Toolkit: A User Guide. *Calphad* **2002**, *26*, 539–553. [CrossRef]
79. Akai, H. Fast Korringa-Kohn-Rostoker Coherent Potential Approximation and Its Application to FCC Ni-Fe Systems. *J. Phys. Condens. Matter* **1989**, *1*, 8045. [CrossRef]
80. Bellaiche, L.; Vanderbilt, D. Virtual Crystal Approximation Revisited: Application to Dielectric and Piezoelectric Properties of Perovskites. *Phys. Rev. B* **2000**, *61*, 7877. [CrossRef]

81. Xia, M.; Record, M.; Boulet, P. Investigation of PbSnTeSe High-Entropy Thermoelectric Alloy. *Materials* **2023**, *16*, 235. [CrossRef] [PubMed]
82. Mishra, S.R.; Karati, A.; Ghosh, S.; Mallik, R.C.; Shabadi, R.; Krishnan, P.S.S.R.; Yadav, S.K.; Ramanujan, R.V.; Murty, B.S. Lowering Thermal Conductivity in Thermoelectric Ti2−xNiCoSnSb Half Heusler High Entropy Alloys. *J. Mater. Sci.* **2023**, *58*, 10736. [CrossRef]
83. Huang, L.F.; Lu, X.Z.; Tennessen, E.; Rondinelli, J.M. An Efficient Ab-Initio Quasiharmonic Approach for the Thermodynamics of Solids. *Comput. Mater. Sci.* **2016**, *120*, 84. [CrossRef]
84. Togo, A.; Tanaka, I. First Principles Phonon Calculations in Materials Science. *Scr. Mater.* **2015**, *108*, 1. [CrossRef]
85. Born, M. On the Stability of Crystal Lattices. I. In *Mathematical Proceedings of the Cambridge Philosophical Society*; Cambridge University Press: Cambridge, UK, 1940; Volume 36, p. 160.
86. Mizokami, K.; Togo, A.; Tanaka, I. Lattice Thermal Conductivities of Two SiO_2 Polymorphs by First-Principles Calculations and the Phonon Boltzmann Transport Equation. *Phys. Rev. B* **2018**, *97*, 224306. [CrossRef]
87. Madsen, G.K.H.; Singh, D.J. BoltzTraP. A Code for Calculating Band-Structure Dependent Quantities. *Comput. Phys. Commun.* **2006**, *175*, 67. [CrossRef]
88. Ma, H.; Li, J.; Yang, G.; Yang, Y.; Mao, X.; Li, C.; Yin, F. Improved Thermoelectric Property of Ti0.75HfMo0.25CrGe by Doping Ti2CrGe Heusler Alloy with Hf and Mo: Confirmation of Entropy "Gene" in Thermoelectric Materials Design. *J. Appl. Phys.* **2018**, *124*, 235104. [CrossRef]
89. Botu, V.; Ramprasad, R. Adaptive Machine Learning Framework to Accelerate Ab Initio Molecular Dynamics. *Int. J. Quantum Chem.* **2015**, *115*, 1074. [CrossRef]
90. Hasan, S.; Adhikari, P.; San, S.; Ching, W.Y. Ab Initio Study of Mechanical and Thermal Properties of GeTe-Based and PbSe-Based High-Entropy Chalcogenides. *Sci. Rep.* **2023**, *13*, 16218. [CrossRef] [PubMed]
91. Reuss, A. Berechnung Der Fließgrenze von Mischkristallen Auf Grund Der Plastizitätsbedingung Für Einkristalle. *ZAMM—J. Appl. Math. Mech./Z. Für Angew. Math. Und Mech.* **1929**, *9*, 49. [CrossRef]
92. Hill, R. The Elastic Behaviour of a Crystalline Aggregate. *Proc. Phys. Soc. Sect. A* **1952**, *65*, 349. [CrossRef]
93. Sun, Z.; Music, D.; Ahuja, R.; Schneider, J.M. Theoretical Investigation of the Bonding and Elastic Properties of Nanolayered Ternary Nitrides. *Phys. Rev. B Condens. Matter Mater. Phys.* **2005**, *71*, 193402. [CrossRef]
94. Saunders, N.; Miodownik, A.P. *CALPHAD (Calculation of Phase Diagrams): A Comprehensive Guide*; Elsevier: Amsterdam, The Netherlands, 1998.
95. Lukas, H.; Fries, S.G.; Sundman, B. *Computational Thermodynamics: The Calphad Method*; Cambridge University Press: Cambridge, UK, 2007.
96. Li, X.; Li, Z.; Chen, C.; Ren, Z.; Wang, C.; Liu, X.; Zhang, Q.; Chen, S. CALPHAD as a Powerful Technique for Design and Fabrication of Thermoelectric Materials. *J. Mater. Chem. A Mater.* **2021**, *9*, 6634. [CrossRef]
97. Berche, A.; Tédenac, J.C.; Jund, P. Phase Separation in the Half-Heusler Thermoelectric Materials (Hf, Ti, Zr) NiSn. *Scr. Mater.* **2017**, *139*, 122. [CrossRef]
98. Borgsmiller, L.; Zavanelli, D.; Snyder, G.J. Phase-Boundary Mapping to Engineer Defects in Thermoelectric Materials. *PRX Energy* **2022**, *1*, 022001. [CrossRef]
99. Ohno, S.; Aydemir, U.; Amsler, M.; Pöhls, J.H.; Chanakian, S.; Zevalkink, A.; White, M.A.; Bux, S.K.; Wolverton, C.; Snyder, G.J. Achieving ZT > 1 in Inexpensive Zintl Phase Ca9Zn4+xSb9 by Phase Boundary Mapping. *Adv. Funct. Mater.* **2017**, *27*, 1606361. [CrossRef]
100. Tang, Y.; Chen, S.; Snyder, G.J. Temperature Dependent Solubility of Yb in Yb–CoSb3 Skutterudite and Its Effect on Preparation, Optimization and Lifetime of Thermoelectrics. *J. Mater.* **2015**, *1*, 75. [CrossRef]
101. Peters, M.C.; Doak, J.W.; Saal, J.E.; Olson, G.B.; Voorhees, P.W. Using First-Principles Calculations in CALPHAD Models to Determine Carrier Concentration of the Binary PbSe Semiconductor. *J. Electron. Mater.* **2019**, *48*, 1031. [CrossRef]
102. Gurunathan, R.; Sarker, S.; Borg, C.K.H.; Saal, J.; Ward, L.; Mehta, A.; Snyder, G.J. Mapping Thermoelectric Transport in a Multicomponent Alloy Space. *Adv. Electron. Mater.* **2022**, *8*, 2200327. [CrossRef]
103. Rickman, J.M.; Chan, H.M.; Harmer, M.P.; Smeltzer, J.A.; Marvel, C.J.; Roy, A.; Balasubramanian, G. Materials Informatics for the Screening of Multi-Principal Elements and High-Entropy Alloys. *Nat. Commun.* **2019**, *10*, 2618. [CrossRef] [PubMed]
104. Xi, J.; Zhu, W.; Li, X.; Jiang, D.; Dronskowski, R.; Shi, X. Discovery of High-Performance Thermoelectric Chalcogenides through Reliable High-Throughput Material Screening. *J. Am. Chem. Soc.* **2018**, *140*, 10785–10793. [CrossRef] [PubMed]
105. Li, R.; Li, X.; Xi, L.; Yang, J.; Singh, D.J.; Zhang, W. High-Throughput Screening for Advanced Thermoelectric Materials: Diamond-Like ABX 2 Compounds. ACS Appl. *Mater. Interfaces* **2019**, *11*, 24859–24866. [CrossRef] [PubMed]
106. Wang, X.; Sheng, Y.; Ning, J.; Xi, J.; Xi, L.; Qiu, D.; Yang, J.; Ke, X. A Critical Review of Machine Learning Techniques on Thermoelectric Materials. *J. Phys. Chem. Lett.* **2023**, *14*, 1808–1822. [CrossRef]
107. Zhang, R.Z.; Gucci, F.; Zhu, H.; Chen, K.; Reece, M.J. Data-Driven Design of Ecofriendly Thermoelectric High-Entropy Sulfides. *Inorg. Chem.* **2018**, *57*, 13027. [CrossRef]
108. Zhang, Z.; Chen, H.; Wei, T.R.; Zhao, K.; Shi, X. Data-Driven Discovery of High-Performance Multicomponent Solid Solution Thermoelectric Materials. *Mater. Today Energy* **2022**, *28*, 101070. [CrossRef]
109. Murdoch, W.J.; Singh, C.; Kumbier, K.; Abbasi-Asl, R.; Yu, B. Definitions, Methods, and Applications in Interpretable Machine Learning. *Proc. Natl. Acad. Sci. USA* **2019**, *116*, 22071. [CrossRef] [PubMed]

110. Li, W.; Liu, M. Interpretable Machine Learning Workflow for Evaluating and Analyzing the Performance of High-Entropy GeTe-Based Thermoelectric Materials. *ACS Appl. Electron. Mater.* **2023**, *5*, 4523. [CrossRef]
111. Lundberg, S.M.; Allen, P.G.; Lee, S.-I. A Unified Approach to Interpreting Model Predictions. *Adv. Neural Inf. Process Syst.* **2017**, *30*, 4768–4777.
112. Zhang, Z.; Zhao, K.; Chen, H.; Ren, Q.; Yue, Z.; Wei, T.R.; Qiu, P.; Chen, L.; Shi, X. Entropy Engineering Induced Exceptional Thermoelectric and Mechanical Performances in Cu2-YAgyTe1-2xSxSex. *Acta Mater.* **2022**, *224*, 117512. [CrossRef]
113. Cai, J.; Wang, H.; Liu, G.; Jiang, J. Designing High Entropy Structure in Thermoelectrics. *Wuji Cailiao Xuebao/J. Inorg. Mater.* **2021**, *36*, 399. [CrossRef]
114. Karthikeyan, V.; Surjadi, J.U.; Li, X.; Fan, R.; Theja, V.C.S.; Li, W.J.; Lu, Y.; Roy, V.A.L. Three Dimensional Architected Thermoelectric Devices with High Toughness and Power Conversion Efficiency. *Nat. Commun.* **2023**, *14*, 2069. [CrossRef]
115. Biswas, K.; He, J.; Blum, I.D.; Wu, C.I.; Hogan, T.P.; Seidman, D.N.; Dravid, V.P.; Kanatzidis, M.G. High-Performance Bulk Thermoelectrics with All-Scale Hierarchical Architectures. *Nature* **2012**, *489*, 414. [CrossRef]